Brodogradnja/Shipbuilding/Open access CrossMark Volume 74 Number 4, 2023

Andi Trimulyono
Muhammad Luqman Hakim
Chairizal Ardhan
Syaiful Tambah Putra Ahmad
Tuswan Tuswan
Ari Wibawa Budi Santosa

http://dx.doi.org/10.21278/brod74403

ISSN 0007-215X
eISSN 1845-5859

Analysis of the double steps position effect on planing hull performances

UDC 629.5.015.2:629.52
Original scientific paper

Summary

Along with developing high-speed craft technology, the planing hull is growing with modifications for better performance. One such technology is stepped hull, both single and double. Planing hull with steps allows the boat to run at a relatively low drag-lift ratio with lower frictional resistance due to reduced wetted area. In this study, the hull was modified with variations in the position of the double steps, which aimed to determine the effect of the first and second step positions on the total resistance, dynamic trim, and dynamic sinkage generated by computational fluid dynamics (CFD). Based on the analysis results, variations in the position of the stepped can change the hull performance. Shortening the distance between the two steps and moving both rearwards toward the transom can lower the total resistance. The dynamic trim and dynamic sinkage decreased as the position of the two steps was shifted further forward. An equation created in a non-dimensional form relates the positions of two steps to the desired results of total resistance, dynamic trim, and dynamic sinkage, namely: $\{(x_1-x_2)/L + (x_1x_2)/(LB)\} \times Fr_\nabla$, where x_1 is distance the first step from transom, x_2 is the distance of the second step, L is the length of the boat, B is the beam of the boat, and Fr_∇ is the volume Froude number.

Key words: *double steps position; planing hull performances; step hull; boat resistance; Computational Fluid Dynamics (CFD)*

1. Introduction

Efforts to decrease emissions on high-speed marine vehicles (HSMVs) are necessary due to their high energy consumption [1], often fueled by fuel oil. These emissions reduction measures are a major focus in the fight against climate change and global warming [2,3], as HSMVs pose a particular challenge. On-board methods to decrease emissions [4,5] include optimizing the hull shape [6–9], utilizing weather routing [10,11], preventing hull roughness caused biofouling [12–21] or coating [22–27], exploring more eco-friendly fuels [28–32], optimizing propellers [33,34], using advanced coating [35–41] and using the energy saving devices [42–45]. Efforts to improve energy efficiency in high-speed marine vehicles must also be considered.

One type of advanced high-speed marine vehicle, especially high-speed craft, experiences planing phenomena. The planing phenomenon occurs because, in addition to the boat's hull moving very fast at a Length Froude number (Fr_L) above 1.2 [46], the hull is specially designed like a prism so that the hydrodynamic flow causes a significant lift force. The hydrodynamic force in the direction along the hull length becomes the ship's resistance (R_T), while the one in the vertical direction becomes the lift force. The hydrodynamic lift force and the hydrostatic force support the boat's weight. What is different from the displacement hull type is that on the planing hull, the value of the hydrodynamic force in the vertical direction is dominant compared with the hydrostatic force [47]. This description is the basis for categorizing hull types, where in the planing hull, the hydrodynamic force is relatively high and has an impact as a lift force. In contrast, the lift force is minimal in the displacement-type hull, where the hydrostatic force is dominant. With this lifting force, the boat's hull is lifted into its equilibrium position. The equilibrium position occurs due to the imbalance in the force on the vertical axis and the moment on the transverse axis of the craft, which will cause sinkage and trim, respectively [48]. As a result of lifting the hull, several values decreased, such as volume displacement, wetted hull area, and wetted length. Reducing these values can reduce the boat's resistance, both frictional resistance and residual resistance. The dominant residual resistance is pressure and wave making resistance.

Planing hull also has several issues and several ways to overcome the issues. Planing hulls can experience dynamic instabilities or operate with a high trim angle in the vertical plane due to the center of pressure being far from the transom. To prevent this, the vessel can be equipped with devices that actively or proactively control the trim angle, or modifications can be made to the hull. Applying a trim control device on a high-speed craft, such as such as interceptor [49–58], trim tab [59–61], the combination of interceptor and trim tab [50,58] [41, 45], and stern foil [62–66], can reduce drag and trim angle. Modifying the hull shape can also reduce the boat's drag, thus improving its performance, such as with a step hull [67] and tunneled hull [68], as examples.

The effect of step hull modification on the performance of planing hull has been widely studied. The stepped hull is a modification of the shape of the hull, in which transverse steps are placed at the bottom, giving the hull the appearance of having two bodies: the forebody and afterbody [69]. Studies using towing tank experiments to analyze the effects of both single step [67,70–77] and double steps [67,69,78–81] have been widely carried out. Taunton et al. [67] conducted experimental tests to study the effect of using a step hull on the performance of high-speed planing-type vessels. In this experimental test using three variations of the model with the same hull, the name of each model is C, C1, C2, where each model has zero, one, and double step hull. According to the tests by Taunton et al. [67], at Fr_∇ around exceed 3.5, the hulls using steps have a lower overall resistance when traveling at the same speed than a hull without using the steps. Savitsky and Morabito [69] conducted an experimental analysis of the longitudinal surface shape profile behind prismatic hulls, including stepped hulls. To provide a better understanding of the effect of implementing the double step in a planing hull, other methods are also being carried out, such as a simplified method [79], the 2D+T method [78], the morphing mesh method [80], the potential flow method [76], the open and pressurized air cavities method [76], CFD with fixed mesh method [74], and CFD with dynamic mesh method [73,75]. Based on the results of previous research, flow separation occurs in the step area which then allows air to enter and makes the area not wet, where this phenomenon can reduce the wetted area and can result in a decrease in the frictional resistance [47,67,69,74,76]. The parameters of the stepped hull each have a unique effect on the resulting boat performance, as discussed by Vitiello et al. [70]. According to Vitiello et al. [70], more steps are needed when the boat's beam is narrower and its speed is lower. The step's height may impact the boat's trim angle. The longitudinal position of the steps affects where the lift force is located, affecting how the boat is trimmed. However, the detailed study of variations in the position of the first and second steps has not been fully studied.

This study will discuss the performance of the effects of modifications in the double-steps position on planing hull based on the findings of the research literature mentioned above. Modifications were made by shifting the position of the step forward and backward, both the first and second steps. The boat performance analyzed is the boat resistance, dynamic trim, and dynamic sinkage obtained using CFD simulations with an unsteady Reynolds-Averaged Navier-Stokes (uRANS) and overset (dynamic) mesh method. The findings of this study are expected to complete the picture of how the position of the double-steps affects the planing boat's performance.

2. Materials and methods

2.1 Hull model preparation

In this study, the research object used was a hull model that a towing tank had experimentally tested by Taunton et al. [67]. The chosen model was the C2 model which has a double step. In this research, the front step was referred to as the first step, and the back step was referred to as the second step. Table 1 describes the model's main particulars, and Fig. 1 and Fig. 2 show the model's generalized representation.

Table 1 The C2 hull model parameters [67]

No	Parameter	Symbol	Value	Unit
1	Length overall	L	2.00	m
2	Beam	B	0.46	m
3	Draught	T	0.09	m
4	Displaced weight	Δ	243.40	N
5	Length overall/ Cube root of the displaced volume	$L/\nabla^{1/3}$	6.86	-
6	Length overall/ Beam	L/B	4.35	-
7	Deadrise angle	β	22.50	degree
8	Longitudinal center of gravity	L_{CG}	0.33	%
9	Keel center of gravity/ Draught	V_{CG}/T	1.10	-
10	The first step position	x_1/L	0.185	-
11	The second step position	x_2/L	0.310	-
12	Steps height/ Length overall	H_s/L	5×10^{-3}	-

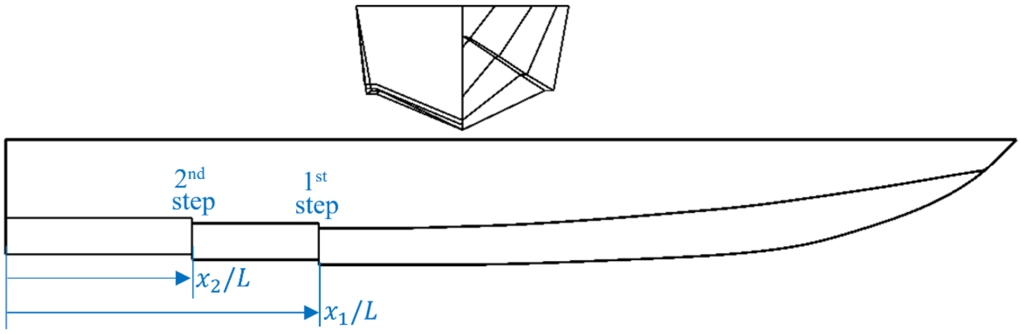

Fig. 1 Lines plan of the C2 model from Taunton et al. [67]

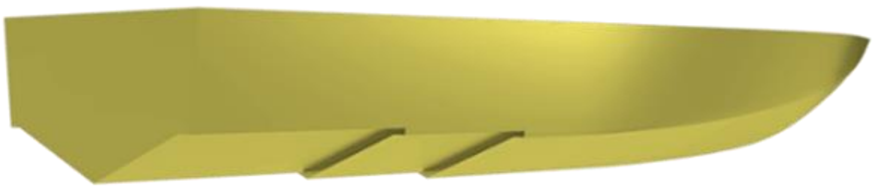

Fig. 2 The 3D view of the C2 model

2.2 Variation of the double-step position

The variation of the model is to shift the position of the first and second steps. The two steps are varied based on the x/L value measured from the transom. The length of these variations is presented in Table 2 and illustrated in Fig. 3. The shifting of these steps impacts changes in the displacement (Δ) value. Therefore, the error difference value of displacement ($\varepsilon\Delta\%$) needs to be explained using Equation (1) and the value is presented in Table 2 as well:

$$\varepsilon\Delta\% = \frac{\Delta_{\mathrm{C2.i}} - \Delta_{\mathrm{C2}}}{\Delta_{\mathrm{C2}}} \times 100\% \quad (1)$$

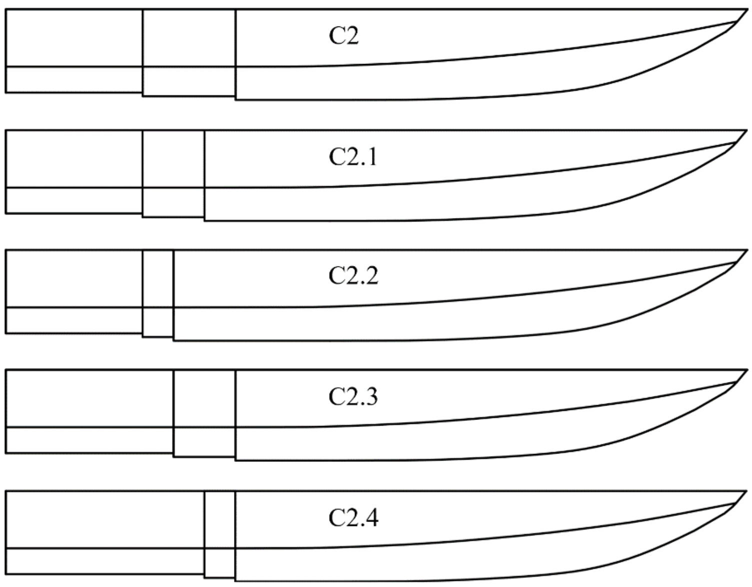

Fig. 3 Illustration of variations in the position of the hull's steps

Table 2 Stepped hull position variations.

Model label	1st step		2nd step		Δ [N]	$\varepsilon\Delta$%
	x_1 (m)	x_1/L	x_2 (m)	x_2/L		
C2	0.620	0.310	0.369	0.185	243.4	0.00
C2.1	0.536	0.268	0.369	0.185	246.0	1.12
C2.2	0.453	0.227	0.369	0.185	248.3	0.92
C2.3	0.620	0.310	0.453	0.227	247.0	1.52
C2.4	0.620	0.310	0.536	0.268	234.7	-0.99

2.3 CFD simulations

2.3.1 Computational setting

This study used an unsteady Reynolds-Averaged Navier-Stokes (uRANS) method to solve the governing equations. The fluid is assumed to be Newtonian and incompressible. When a fluid is assumed to be Newtonian, it means that the fluid viscosity is considered constant [82]. On the other hand, when a fluid is assumed to be incompressible, it means that the fluid density is considered constant throughout the simulation [82]. The conservation of mass and momentum equations are solved with commercial CFD software STAR CCM+. The average continuity and momentum equations are given in Equations (2) and (3). Where: U_i is the average speed component; $\bar{P}$ is the average pressure; ρ is the effective density of the fluid; μ is the effective viscosity; u_i' is the fluctuation velocity component; $\rho\overline{U_i'U_j'}$ is the Reynolds stress, $\overline{\tau_{ij}}$ is the tensor component of the mean viscous stress [83], as given in Equation (4):

$$\frac{\partial(\rho\bar{U}_i)}{\partial x_i}=0 \tag{2}$$

$$\frac{\partial(\rho\bar{U}_i)}{\partial t}+\frac{\partial}{\partial x_i}\left(\rho\bar{U}_i\bar{U}_j+\rho\overline{U_i'U_j'}\right)=-\frac{\partial\bar{P}}{\partial x_i}+\frac{\partial\overline{\tau_{ij}}}{\partial x_j} \tag{3}$$

$$\tau_{ij}=\mu\left(\frac{\partial\bar{U}_i}{\partial x_j}+\frac{\partial\bar{U}_j}{\partial x_i}\right) \tag{4}$$

This simulation employed the VOF (volume of fluid) method to depict the impact of a free surface on the computational model. The VOF technique was appropriate for modeling multiple distinct flow phases. The water and air fluid functions rely on the volume fraction attribute in Equation (5), where V represents the designated calculation area, V_1 corresponds to the volume of fluid 1, and V_2 represents the volume of fluid 2. Each grid is assumed to have a volume fraction value of either 1 or 0 to differentiate between the air and water fluids [84]:

$$\alpha(\vec{x},t)=\begin{cases}\Delta_1,\vec{x},\in V_1\\ \Delta_2,\vec{x},\in V_2\end{cases} \tag{5}$$

The continuity equations for volume fraction describe the conservation of mass for each component in a mixture. For two-phase flow, the continuity equation for each phase can be written as in Equations (6) and (8). Where: α_1 and α_2 are the volume fractions of the first and second fluids, respectively; ρ_1 and ρ_2 are the densities of the first and second fluids, respectively; $\bar{U}$ is the boat's speed; and ∇ is the divergence operator. The VOF C_{ijk} function is an integral of $\alpha(\vec{x},t)$ on each grid cell in each volume cell as described in Equation (8) which became Equation (9). Where: C = 1 for the grid that defined the fluid; C = 0, indicating that the grid comprised a mixture of water and air phases under the air phase and when 0 < C < 1:

$$\frac{\partial(\alpha_1\rho_1)}{\partial t} + \overline{U} \cdot \nabla(\alpha_1\rho_1) = 0 \tag{6}$$

$$\frac{\partial(\alpha_2\rho_2)}{\partial t} + \overline{U} \cdot \nabla(\alpha_2\rho_2) = 0 \tag{7}$$

$$C_{ijk} = \frac{1}{\Delta V_{ijk}} \int \alpha(\vec{x},t)dV \tag{8}$$

$$\frac{\partial C}{\partial t} + \overline{U} \cdot \nabla C = 0 \tag{9}$$

The realizable $k-\varepsilon$ (epsilon) turbulence model with a standard wall function, which relates the Reynolds stress to the average flow property, was used to approximate the system of Equations (2) and (3). This turbulence model has two equations representing the turbulence kinetic energy transport k and the turbulence dissipation rate ε [85].

A time-step determination needs to be considered in simulations with an unsteady flow. The time step is defined as the period interval for each iteration calculation. The time step value is related to the Courant-Frederich-Lewis (CFL) number to ensure the stability of numerical calculations. Determining the time-step value in this CFD simulation follows the procedure from ITTC [86], where it is a function of the length and speed of the craft (see Equation (10)). The faster the boat's speed, the smaller the time-step value used. Determining the value of this time step is also very important to capture dynamic phenomena because this simulation uses a dynamic mesh, where the hull model can trim and heave dynamically:

$$\Delta t = 0.005\text{~}0.01\,\frac{L}{V_s} \tag{10}$$

2.3.2 Domain and boundary condition settings

The creation of a computing domain is described in this subsection. The domain settings are domain size and boundary conditions. The size of the domain formed is depicted in Fig. 4, where the size is based on the length of the simulated boat model and is based on work done by Lotfi et al. [74]. The setting of the boundary conditions is described in Fig. 4. The simulation uses a multi-fluid in the presence of a water surface as a free surface. So that the inlet and outlet are arranged so that there are two fluids, namely air, and water.

The type of boundary conditions must be set correctly for the numerical simulation to run appropriately. The inlet, top, bottom, and side boundary conditions are conditioned as velocity inlets. The inlet section is used as a passage for water and air to enter at a predetermined speed to simulate a speeding boat. In the outlet section, boundary conditions are defined as pressure outlets with a field function of hydrostatic pressure. In addition, a symmetry boundary condition is applied as a Symmetry Plane in the middle plane and a no-slip condition on the hull model surface. This simulation uses a multiphase model of water and air to predict wave patterns on the free surface. The $k-\varepsilon$ model is used to consider turbulent flow effects. The simulation is completed on only half of the hull to reduce computational costs.

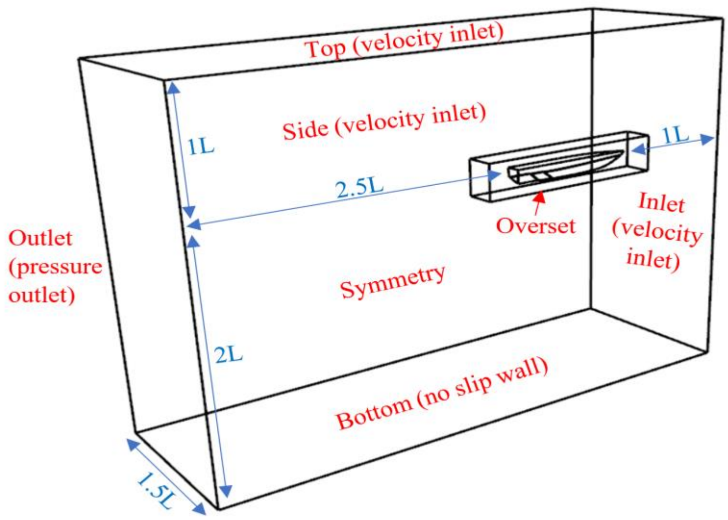

Fig. 4 Domain size and boundary condition settings

2.3.3 Mesh generation

The settings for preparing the mesh are described in this subsection. Mesh refinement focuses on objects and water surfaces to shorten computation time while getting accurate results. The objects were refined on the hull and the area around the hull. The refinement is carried out using the anisotropic mesh method, which aims to focus the mesh on the *x*, *y*, or *z*-axis ordinate. The refinement results obtained three variations in the number of elements, namely coarse, medium, and fine arrangement, each producing a number of elements of 1.3 M, 2.9 M, and 5.9 M, respectively. Fig. 5 shows the arrangement of the medium arrangement mesh with many elements of 2.9 M.

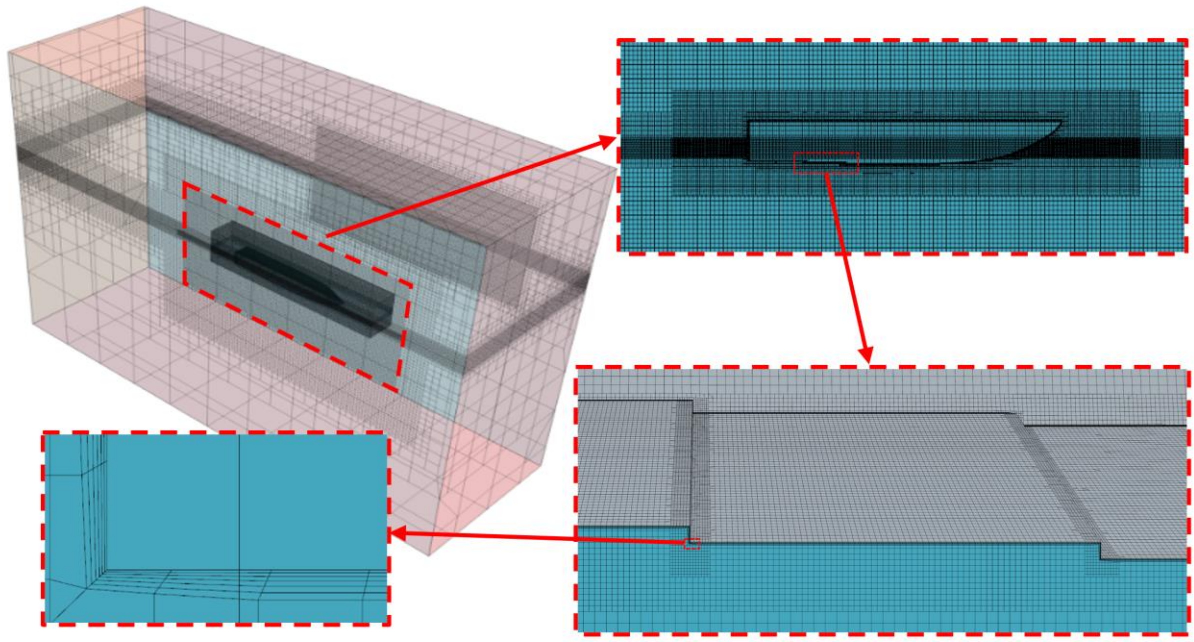

Fig. 5 The result of mesh arrangement with the refinement at free surface area, steps of hull area, and inflation layer at the wall

The dynamic mesh was used to simulate boat motion using dynamic fluid-body interaction (DFBI) by combining two degrees of freedom: free heave and trim. The study utilized a rigid body's motion and an overset grid system to depict the movement of the boat in the fluid domain. The translational (sinkage) and rotational (trim) motions at the center of mass of the boat model are simulated based on Equations (11) and (12), respectively [51,76]. The equations involve several variables: M, which represents the net moment acting on the boat model for y-axis rotation; I, the moment of inertia for y-axis rotation; ω, the angular velocity of the boat for y-axis rotation; m, the mass of the boat; F, the net force acting on the surface of the boat for z-axis translation; and U, the speed of the boat. The forces and moments acting on the boat were obtained from fluid pressure and shear forces on the surface of the boat:

$$I\frac{d\omega}{dt} = \sum M \tag{11}$$

$$m\frac{dU}{dt} = \sum F \tag{12}$$

The dynamic mesh simulation method was used for these simulations, namely overset mesh method. The Overset mesh method has been proven to be more efficient in handling complex movements. This technique enables the use of multiple overlapping meshes to handle the complex motion of planing hull boats. Moreover, the Overset mesh method can provide higher accuracy in simulations since the moving mesh can adjust to the motion of the planing craft [87], minimizing numerical errors. Some examples of works that use the overset mesh method in planing craft simulation as done by De Marco et al. [73], Di Caterino et al. [75], Hosseini et al. [87], Samuel et al. [51] and more. The simulation results using the dynamic mesh method are closer to the results from the experiment than the static mesh method [88]. In the overset mesh method, the domain modeling is divided into two parts: the background geometry part as a donor and the overset geometry part as an acceptor. It should be noted that in the overset mesh method, the mesh density of the donor and acceptor must be of the same dimension, or there is no significant difference. Differences in dimensions that are too large can cause data transfer errors, so the simulation cannot be continued [89].

Determining the y^+ is very important in CFD simulations using the turbulence model [90]. For turbulence models using the wall function method, the recommended y^+ is above 30 to avoid the buffer area, and it must be right in the log law area of the boundary layer structure. In this study, y^+ was used with a value of 50. The y^+ was between 45 – 60 to get accurate simulation results [91]. According to ITTC, the calculation of the y^+ value is obtained through Equation (13) [86], where: y is the thickness of the first layer that must be adjusted in making the mesh arrangement, L is the length of the hull, Re is the value of the Reynolds number, and C_f is the skin friction coefficient of the object that can use Empirical formula from ITTC'57 [92]. Therefore, to get the desired y^+ value, the first mesh distance to the wall must be adjusted:

$$\frac{y}{L} = \frac{y^+}{Re\sqrt{C_f/2}} \tag{13}$$

The way to set this distance is to apply an inflation layer mesh. Fig. 5 shows the implementation of the inflation layer mesh in this numerical model.

3. Result and discussion

3.1 Verification study

To evaluate the potential inaccuracies in both space and time of the simulations, convergence studies were conducted. In order to estimate the numerical uncertainties, the Grid Convergence Index (GCI) method based on Generalized Richardson Extrapolation [93]. The GCI method involves calculating the ratio of the error between two different grid resolutions, which provides valuable information about the rate at which the error decreases as the resolution increases. According to Celik et al. [94], the sequence of calculation for this method is as follows:

$$p_a = \frac{1}{\ln(r_{21})}\left|\ln\left|\frac{\varepsilon_{32}}{\varepsilon_{21}}\right| + q(p_a)\right| \tag{14}$$

$$q(p_a) = \ln\left(\frac{r_{21}^{p_a} - s}{r_{32}^{p_a} - s}\right) \tag{15}$$

$$s = \text{sign}\left(\frac{\varepsilon_{32}}{\varepsilon_{21}}\right) \tag{16}$$

where, r_{21} and r_{32} are refinement factors given by $r_{21} = \sqrt[3]{N_1/N_2}$ for a spatial convergence study of a 3D model. convergence study. N_i are the cell number. $\varepsilon_{32} = \emptyset_3 - \emptyset_2$, $\varepsilon_{21} = \emptyset_2 - \emptyset_1$, and $\emptyset_i$ denotes the simulation result, i.e., R_T/Δ in this study.

The extrapolated value is calculated by:

$$\emptyset_{ext}^{21} = \frac{r_{21}^{p}\emptyset_1 - \emptyset_2}{r_{21}^{p} - 1} \tag{17}$$

The approximate relative error, e_a^{21}, is obtained by:

$$e_a^{21} = \left|\frac{\emptyset_1 - \emptyset_2}{\emptyset_1}\right| \tag{18}$$

The extrapolated relative error, e_{ext}^{21}, is obtained by:

$$e_{ext}^{21} = \left|\frac{\emptyset_{ext}^{21} - \emptyset_1}{\emptyset_{ext}^{21}}\right| \tag{19}$$

Finally, the fine-grid convergence index is found by

$$GCI_{fine}^{21} = \frac{1.25 e_a^{21}}{r_{21}^{p} - 1} \tag{20}$$

The result of numerical uncertainty calculation was obtained as 1.25%, with the detailed calculation shown in Table 3.

Table 3 Parameters used for the calculation of the discretization error for the spatial convergence study, key variable: R_T/Δ of C2 model simulation at Fr_∇ 4.81 (8.13 m/s)

N_1 (Coarse)	1.3×10^6	ε_{32}	-0.017
N_2 (Medium)	2.9×10^6	ε_{21}	-0.007
N_3 (Fine)	5.9×10^6	s	1
r_{21}	1.329	e_a^{21}	0.003
r_{32}	1.260	q	0.237
$\emptyset_1$	2.117	p_a	3.948
$\emptyset_2$	2.110	$\emptyset_{ext}^{21}$	2.138
$\emptyset_3$	2.094	e_{ext}^{21}	0.99%
		GCI_{fine}^{21}	1.25%

3.2 Validation Study

A validation test was carried out by comparing the CFD simulation results with the results of experimental testing conducted by Taunton et al. [67]. Errors are calculated using Equation (21) to assess the precision of current CFD results. The term ψ in this context refers to any of the three parameters that are being validated, namely R_T/Δ for the resistance, θ_V for dynamic trim, and $Z_V/\nabla^{(1/3)}$ for dynamic sinkage. Experimental and numerical data are indicated by the subscripts EXP and CFD, respectively. Equation (22) calculates RMSE (Root Mean Square Error), which measures the errors of the samples based on the speed variations:

$$E_\psi\% = \frac{\psi_{CFD} - \psi_{EXP}}{\psi_{EXP}} \times 100\% \tag{21}$$

$$\text{RSME} = \sqrt{\sum_{i=1}^{N} \frac{(E^2)}{N}} \tag{22}$$

Fig. 6 shows a sample of the convergence of the results. The results were generated using the C2 model and correspond to a Froude number of 4.81 (flow velocity of 8.13 m/s). The time histories plotted in the figure indicate that all data converges after 2 seconds, and the simulation is stopped at 5 seconds. As such, the results obtained were the average values of the real-time data collected between *t* = 2 seconds and *t* = 5 seconds.

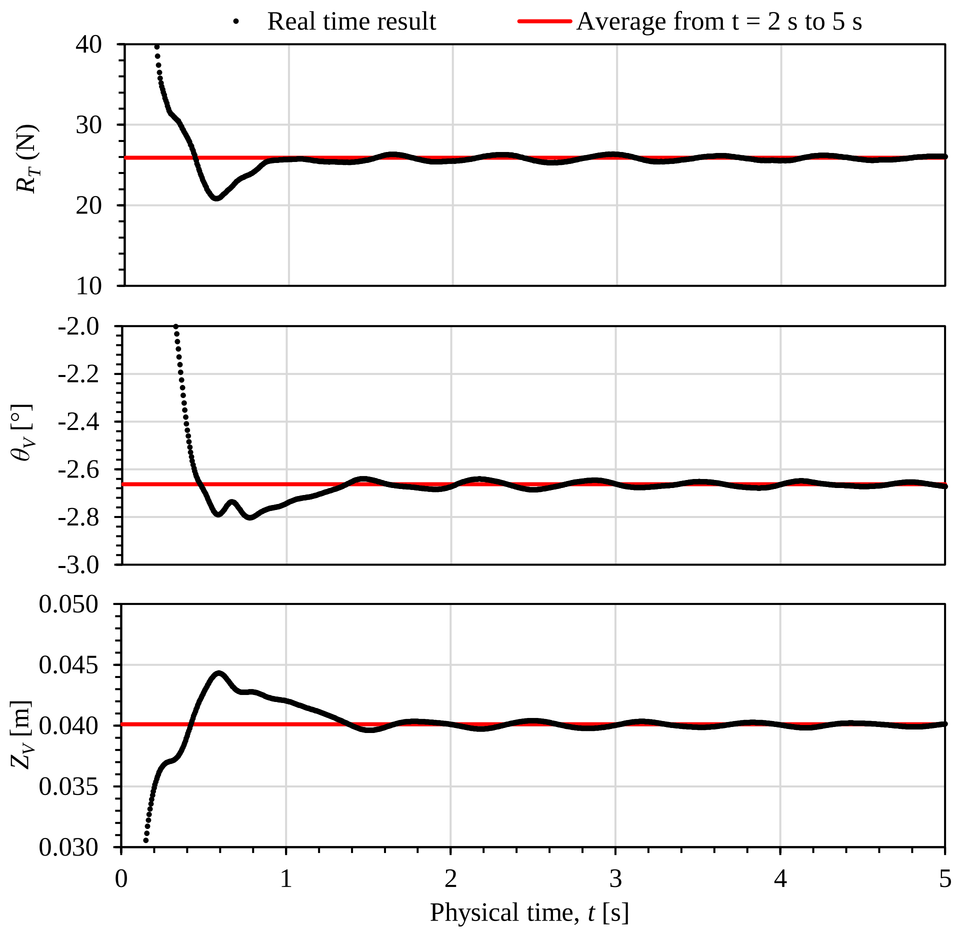

Fig. 6 A sample of convergence of the resistance, trim, and sinkage results, showing how a CFD model calculates the equilibrium condition of the C2 model and correspond to Fr_∇ 4.81 (8.13 m/s)

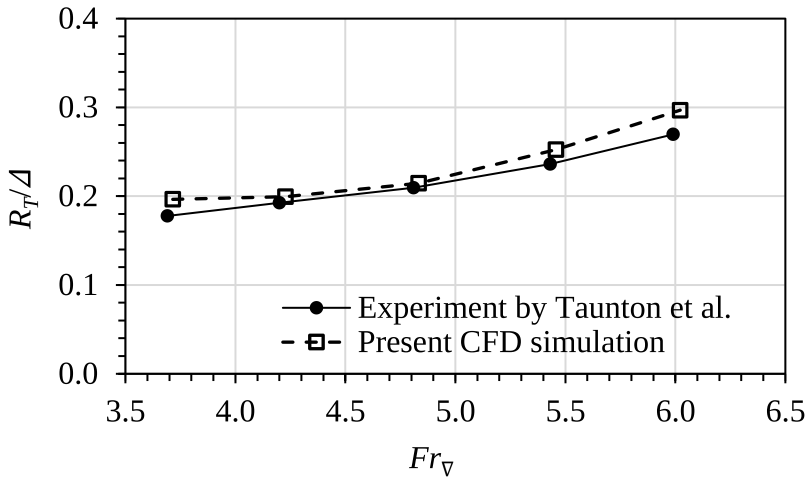

Fig. 7 Comparison of the resistance results obtained from the present CFD simulation with the experimental results from Taunton et al. [67]

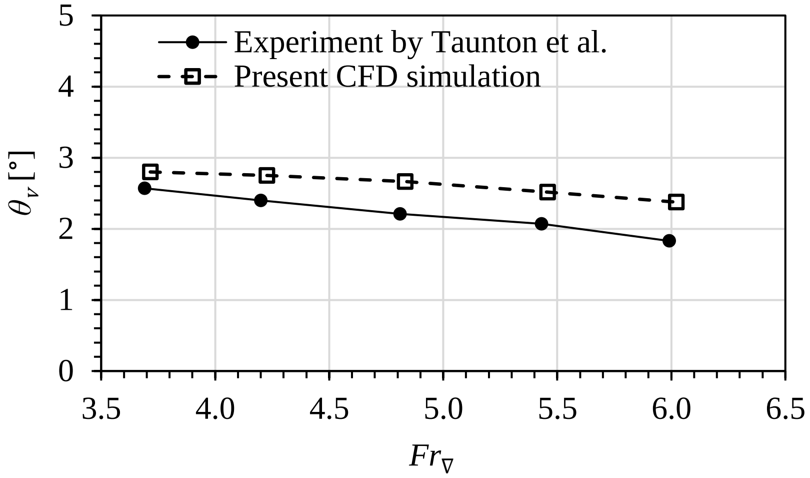

Fig. 8 Comparison of the dynamic trim results obtained from the present CFD simulation with the experimental results from Taunton et al. [67]

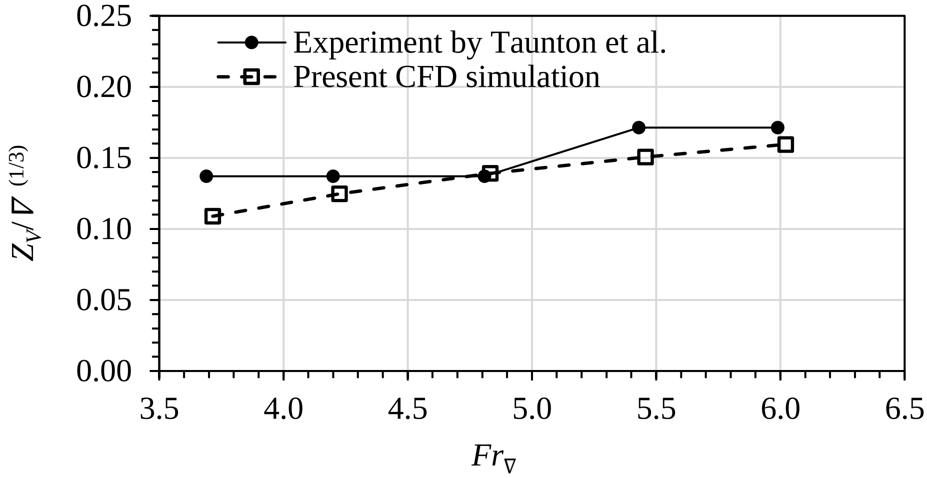

Fig. 9 Comparison of the dynamic sinkage results obtained from the present CFD simulation with the experimental results from Taunton et al. [67]

Table 4 Summary of the errors of different CFD models used in the current research

Speed [m/s]	E_{Fr_∇}%	$E_{R_T/\Delta}$%	E_{θ_V}%	$E_{Z_V/\nabla^{(1/3)}}$%
6.25	0.69	10.54	8.93	-20.51
7.11	0.63	3.61	14.60	-8.98
8.13	0.48	2.45	20.48	1.46
9.18	0.50	6.77	21.56	-12.07
10.13	0.53	10.12	29.81	-6.88
RMSE	0.57	7.46	20.33	11.80

The validation findings showed that, although not flawless, the outcomes are acceptable. Graphical comparisons of the CFD and experimental results are presented in Fig. 7, Fig. 8, and Fig. 9, with the corresponding RMSE values provided in Table 4. Fig. 7 reveals a slight difference in resistance results between the CFD simulation and the experiment, with an RMSE value of 7.46%. In Fig. 8, the dynamic trim results display a quite different, with an RMSE value of 20.33%. The dynamic sinkage results in Fig. 9 are also slightly different, but with an RMSE value of 11.8%. It should be noted that the validation of dynamic trim and sinkage results is challenging, as description by Lotfi et al. [74], Dashtimanesh et al. [80], and Hosseini et al. [87].

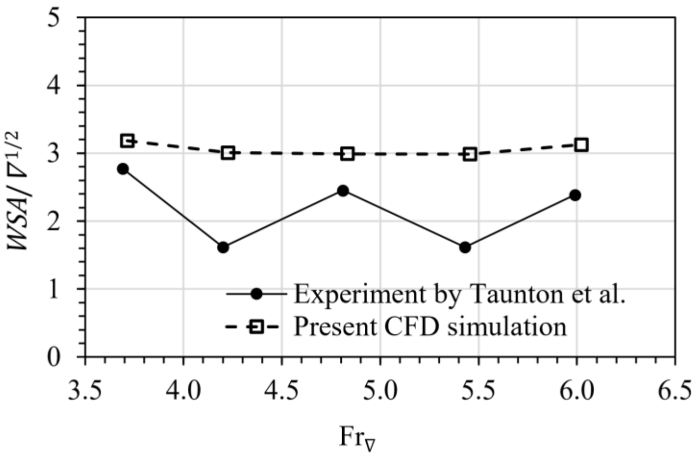

Fig. 10 Comparison of the wetted surface area results obtained from the present CFD simulation with the experimental results from Taunton et al. [67]

The validation results revealed a substantial error due to the assumption of the moment of inertia value input into the model. The moment of inertia value is based on the recommendation from ITTC [95]. From the validation analysis of the trim, it appears that the trim value in the CFD simulation is currently too high, and the lift (heave) value is lower than the experimental results. This indicates a higher value of wetted surface area than the experimental results, as seen in Fig. 10. Therefore, it is estimated that the frictional resistance value is too high in the experimental results. Nevertheless, the authors decided to continue the study and focus on the effects of variations in the double step position in the research results.

3.3 Uncertainty Analysis

To calculate the uncertainty value (U_V) in this analysis, the method from ITTC [96] was used. The U_V value was calculated using the following Equation:

$$U_V^2 = U_D^2 + U_{SN}^2 \tag{23}$$

where U_D represents the uncertainty of the experimental results, and U_{SN} represents the numerical uncertainty. Based on Taunton et al. [67], the experimental uncertainty is ~10%. According to the section of Verification study, the value of U_{SN} is 1.25%. Thus, using Equation (23), the uncertainty value for this analysis was U_V = 10.08%. According to ITTC [96], validation is considered successful if $|E| < U_V$. The value of $|E|$ is the comparison value calculated in the section of Validation study, which was found to be 7.46%. Therefore, validation is achieved as $|E| < U_V$.

3.4 Total resistance results

Analysis of the CFD simulation for resistance results is described in this subsection. The graph in Fig. 11 illustrates the overall resistance results of all model modifications. Analysis of the effect of the position of the first step and the second step on the resistance results is described in Fig. 12.

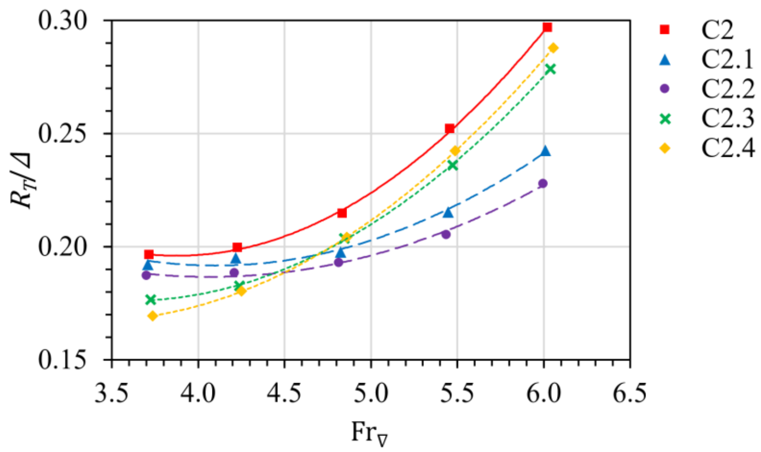

Fig. 11 Resistance results for all model variations

Fig. 11 describes the resistance results for all model variations based on the Fr_∇ value. All resistance results showed that the higher the Fr_∇ or boat speed, the higher the resistance. Then, all changes in step position, whether the first or second step, showed a lower resistance than the original model, namely model C2. Model C2.4 had the lowest resistance value for speeds at Fr_∇ below 4.7s, while model C2.2 had the lowest resistance at Fr_∇ above 4.7s.

Several model variations showed different trends of the changes in the resistance based on the Fr_∇ value. First, the comparison resistance results of models C2, C2.1, and C2.2, where the three models had a different first step position, and the second step was the same. It can be seen that C2.2 had lower boat resistance than C2.1 and C2 models. The trend of increasing resistance based on Fr_∇ showed that models C2.1 and C2.2 were lower slopes than C2. These results indicated that changing the position of the first step will effectively reduce resistance at high speeds (Fr_∇). Second, the comparison results of the models C2, C2.3, and C2.4, where they had a different second step position, but the first step was the same. It can be seen that C2.3 had lower boat resistance than C2.4 and C2 models at Fr_∇ above 4.8s, but at Fr_∇ below 4.8s, the C2.4 was the lowest. The trend of increasing resistance based on Fr_∇ showed that models C2 and C2.3 were similar, while the trend from C2.4 was slightly different. These results indicated that changing the position of the second step will effectively reduce resistance at low speeds (Fr_∇).

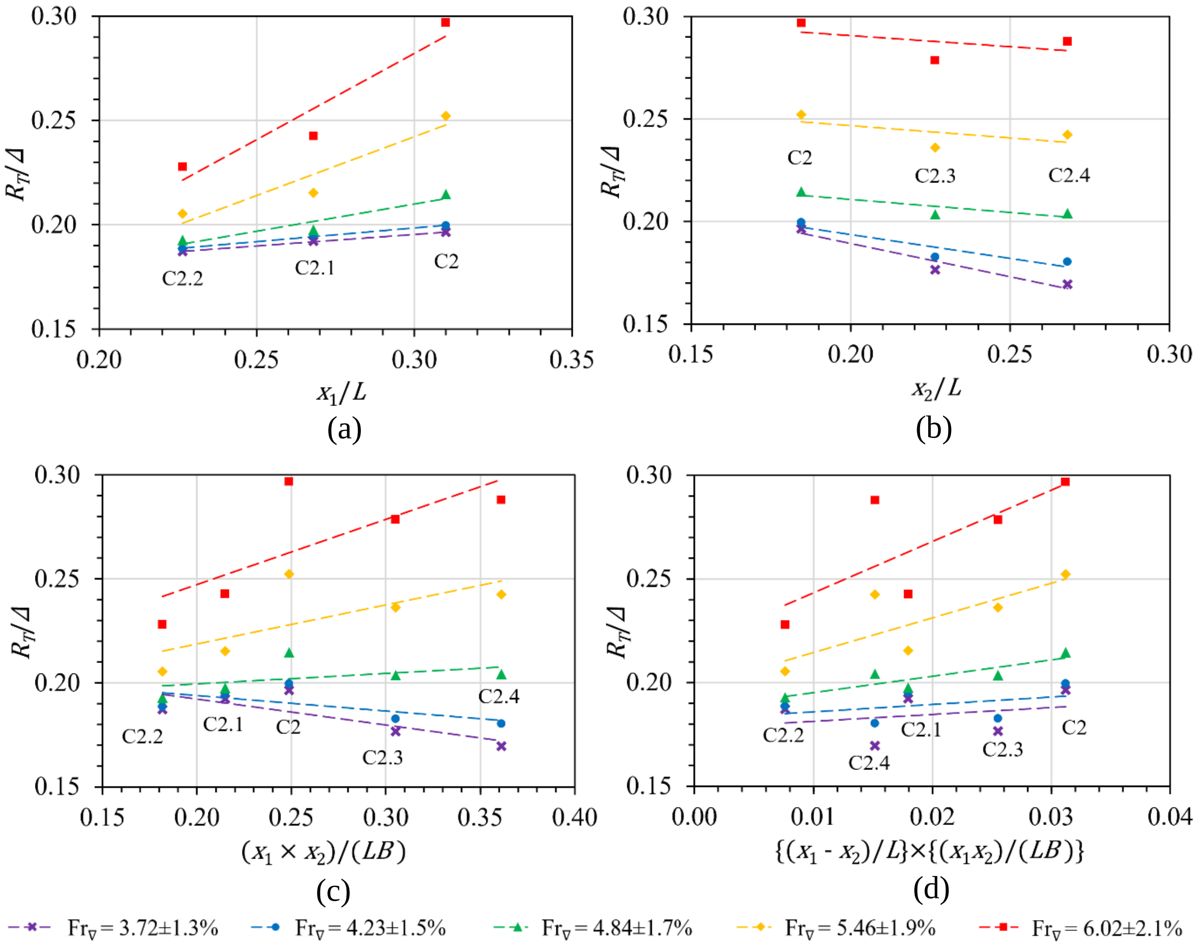

Fig. 12 The graphs plot the resistance against the position of the hull steps: (a) first step only, (b) second step only, (c) the multiplication of the two steps, and (d) the difference between the two steps times the multiplication of the two steps

Fig. 12 explains how the two steps' positions affected the outcomes of boat resistance. Fig. 12 (a) showed that the boat's resistance increased with the first step's forwardness. In contrast, if the position of the second step was getting more forward, the resistance became a bit smaller, as shown in Fig. 12 (b). The graph in Fig. 12 (c) showed that the effect of multiplying the position of the two steps was inconsistent based on the speed value, where at a lower speed (Fr_∇), the higher the multiplication of the two steps, the resistance decreases. Still, at high speed, the opposite occurred. This result corresponded to the results expressed by Vitiello et al. [70] and Najafi et al. [71], where shifting the step further forward will reduce the drag. Therefore, the authors tried to add the effect of the distance between the two steps, plotted in Fig. 12 (d). Based on the plot, the higher the value of the distance of the two steps multiplied by the multiplication of the two steps, the resistance was higher.

The author attempted to find the relationship between the position of the two steps, distance between the steps, and boat speed, which was then obtained and explained in Fig. 13. The curve shows the relationship between the three variations made. The distance between the two steps is represented by $x_1 - x_2$, and the position of the both steps is represented by the multiplication of x_1 and x_2. All parameters were made into nondimensional form. The regression results showed an acceptable value, with a determination coefficient of R^2 = 0.5779 and a slope of 0.059.

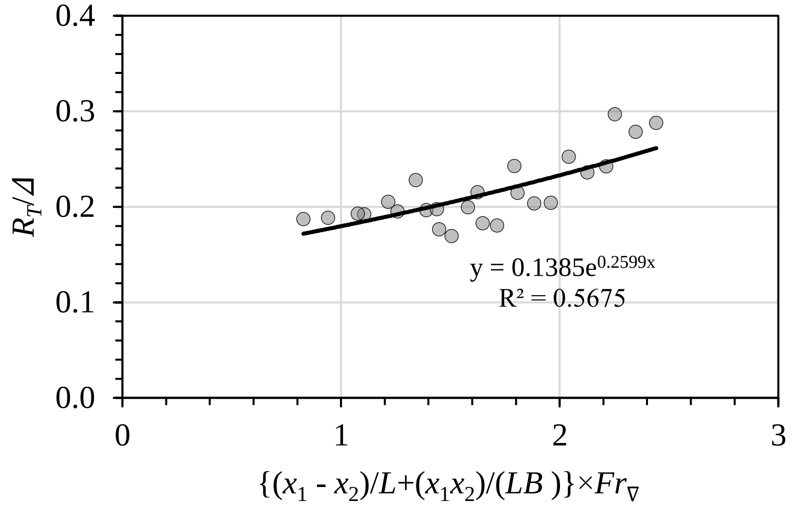

Fig. 13 Regression analysis of the relationship between the distance and the location of the double step, as well as the speed parameters to the total resistance result

3.5 Frictional and residual resistances results

This chapter discusses the resistance results in more detail, down to the components of resistance, such as frictional resistance, residual resistance, pressure resistance, and wave-making resistance. The difference between frictional resistance and the ratio of frictional resistance to residual resistance is shown in Fig. 14. Fig. 15 to Fig. 17 describe the distribution of the wall shear stress X contour on all models, taken at a velocity of 10.13 m/s (Fr_∇ = 6.01). Fig. 18 and Fig. 19 show the local value of wall shear stress X on the centerline section and 1/4B section for each model, taken at a velocity of 10.13 m/s (Fr_∇ = 6.01). Fig. 20 visualizes the flow separation that causes air to be trapped behind the step, decreasing frictional resistance and even reversing its direction (pushing the boat forward).

Based on the analysis results in Fig. 14 (a) and (b), it was found that the position of the steps and the distance between the two steps greatly affected the frictional resistance results. Model C2.2 produced the smallest frictional resistance among the other models at high speeds. As described in Fig. 12 (c) and (d), Model C2.2 had the furthest back step position compared to the other models. The distance between the first and second steps in Model C2.2 was also the closest compared to the other models. This was further reinforced by the trim value results of Model C2.2 being the highest, which will be explained in the subsection 3.5 Dynamic trim results. The dynamic sinkage value of Model C2.2 was also the highest, based on the dynamic sinkage results explained in the subsection 3.6 Dynamic sinkage result. This made the wetted length of C2.2 suspected to be shorter than the other models. This phenomenon was reinforced in the plot in Fig. 18 and Fig. 19, where it can be seen that the local wall shear stress value of Model C2.2 was the lowest at the front of both steps and the back of the steps. This was different from Model C2 and C2.4, where they produced the high frictional resistance for the area in front of both steps and at the back of the steps. This phenomenon occurred in both the centerline and ¼ beam of the hull.

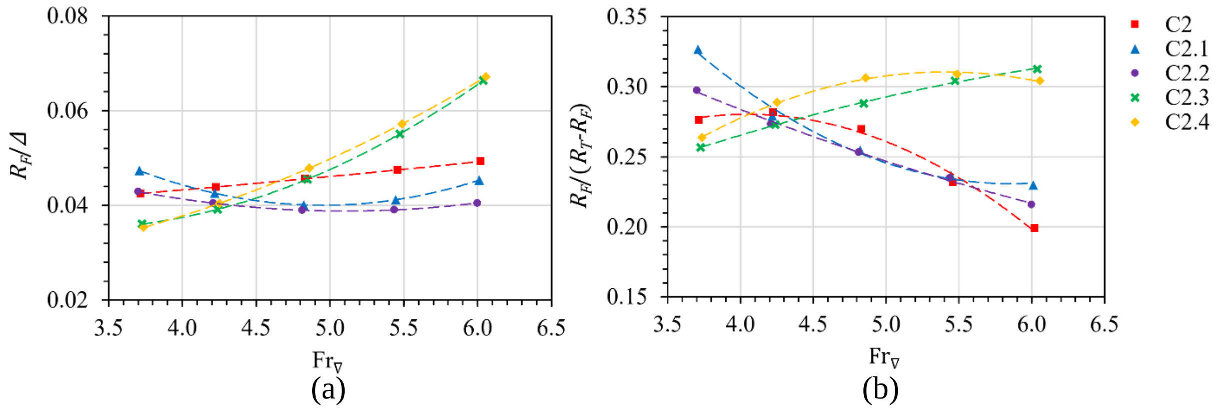

Fig. 14 Comparison of the results of frictional resistance of all models: (a) frictional resistance to displacement, and (b) frictional resistance to residual resistance

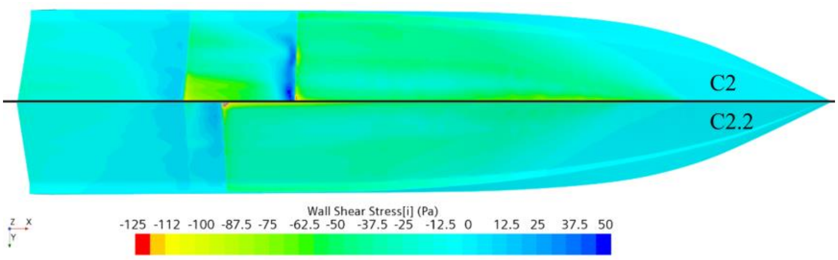

Fig. 15 Comparison of wall shear stress distribution for C2 and C2.2 models at 10.13 m/s (Fr_∇ = 6.01)

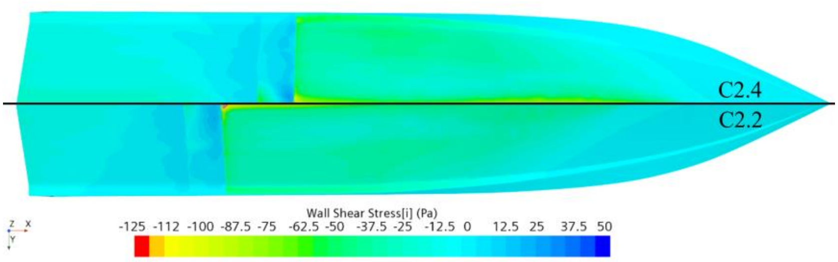

Fig. 16 Comparison of wall shear stress distribution for C2.2 and C2.4 models at 10.13 m/s (Fr_∇ = 6.01)

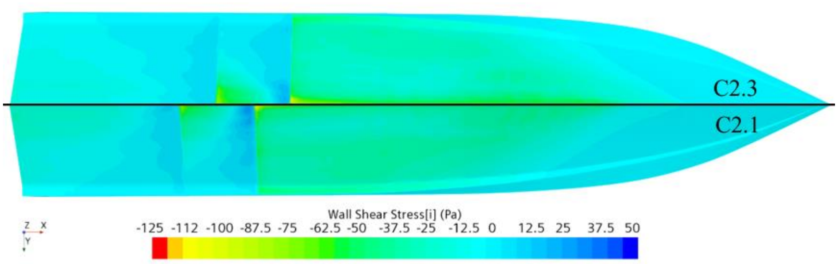

Fig. 17 Comparison of wall shear stress distribution for C2.1 and C2.3 models at 10.13 m/s (Fr_∇ = 6.01)

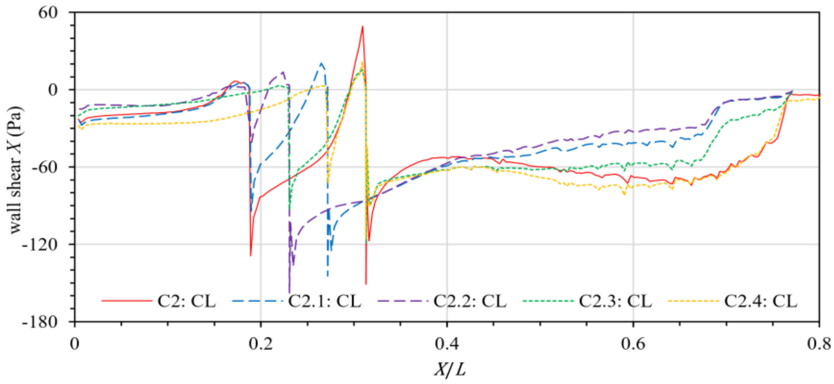

Fig. 18 Comparison of local wall shear *X* values of each model on the centerline

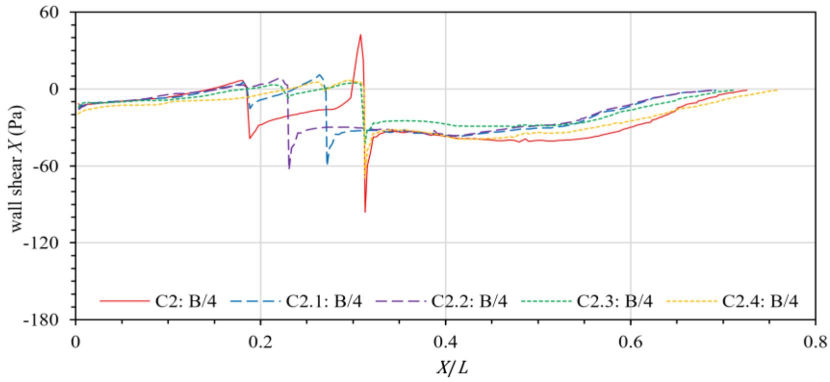

Fig. 19 Comparison of local wall shear *X* values of each model on the ¼ *B*

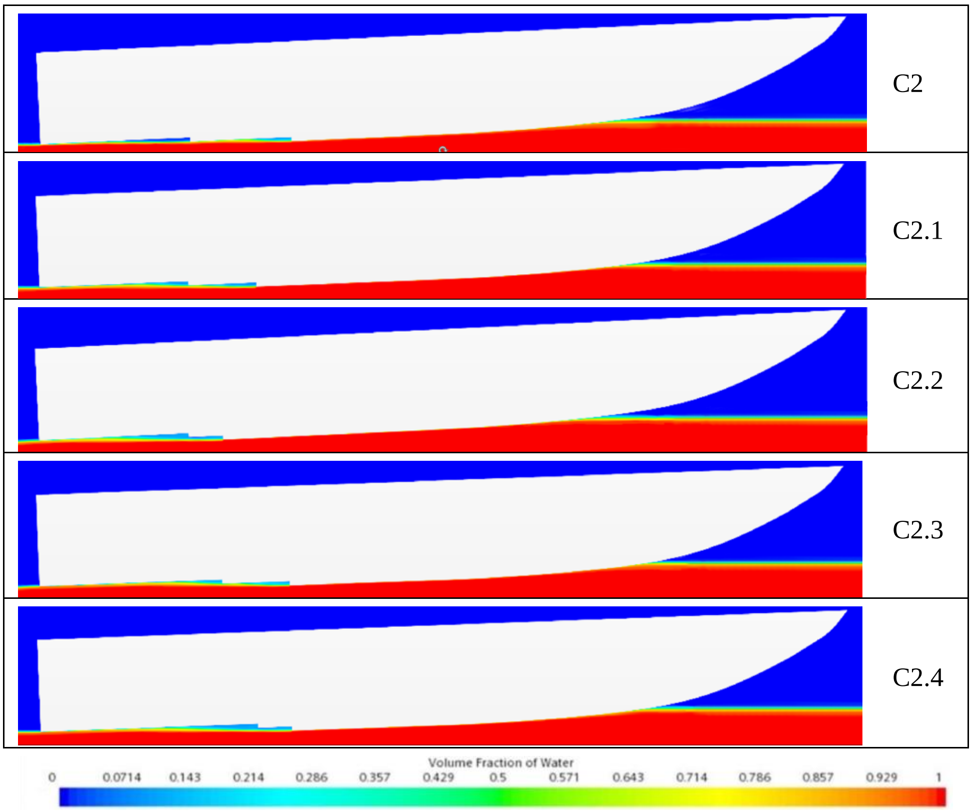

Fig. 20 Comparison of separation length results for all variations at 10.13 m/s (Fr_∇ = 6.01)

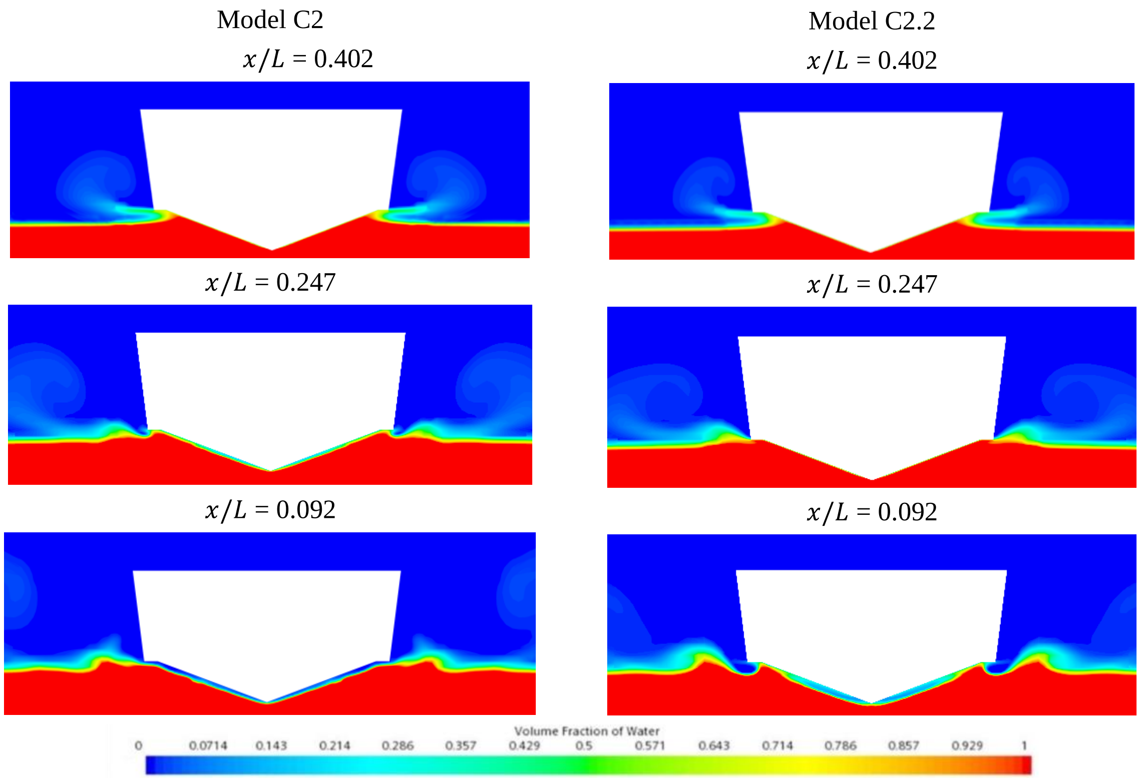

Fig. 21 Volume fraction of water in the cross-section of Model C2 and C2.2 that taken before the first step, between the two steps, and after the second step (Fr_∇ = 6.01)

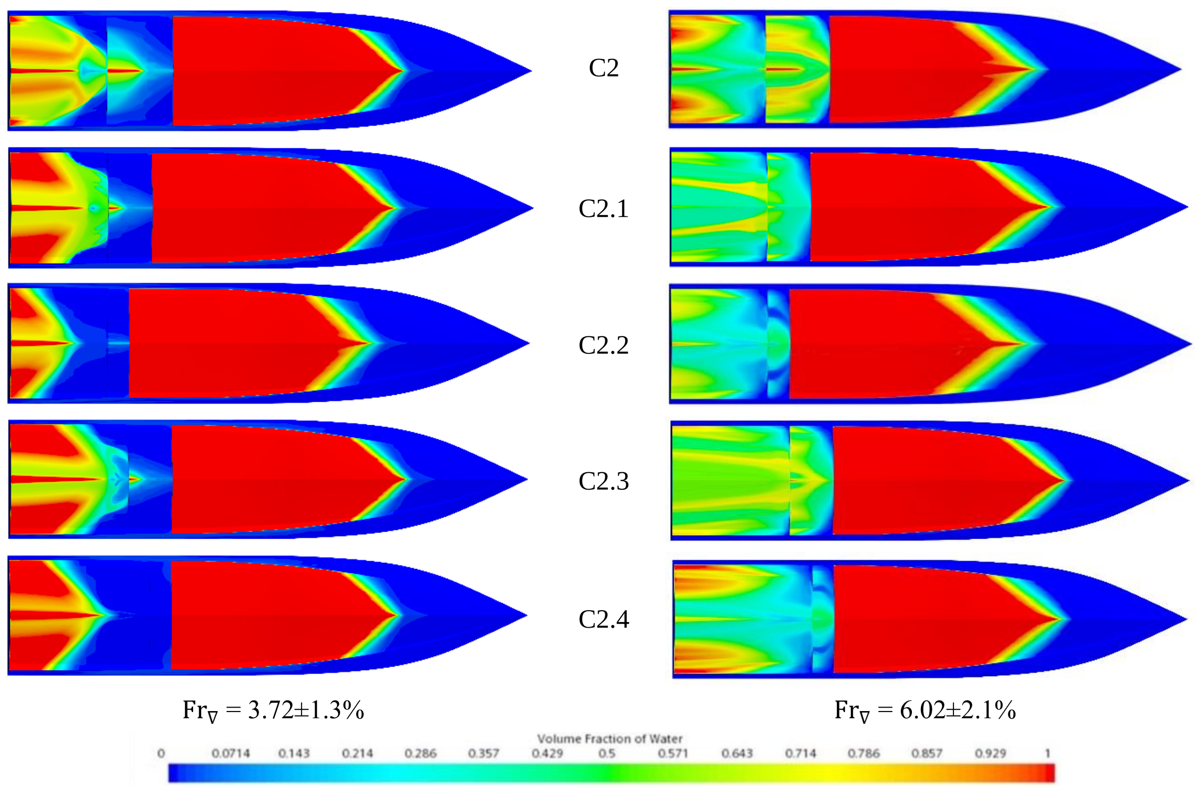

Fig. 22 Comparison of volume fraction of water to determine the wetted surface area

Fig. 20 compares the separation length of all models from the plot of volume fraction results. It is then possible to see how an air cavity was created once the flow had passed through the steps. The result from model C2.2 shows that the air cavity appeared slightly bluer (higher) compared to model C2, indicating that the air cavity of model C2.2 is higher than that in model C2. This result was also evidenced by the negative pressure results shown in Fig. 24. With the negative pressure, the air cavities were created and will reduce the wall shear stress value because of the difference in the density of water and air. The wall shear stress contour was compared in Fig. 15, where model C2.2 had a slightly wider yellow color pattern (zero shear value) than model C2.

Fig. 21 shows the contour of the volume fraction of water in the cross-section of Model C2 and C2.2. The cross-sections are taken before the first step, between the two steps, and after the second step. It can be seen that in the cross-section before the first step, x/L = 0.402, both Model C2 and Model C2.2 do not have any air cavity, indicated by the dark blue contour on the bottom. Then, in the cross-section between the two steps, x/L = 0.247, Model C2.2 already shows an air cavity near the chine, but it is not yet visible in Model C2. Only in the cross-section after the second step, x/L = 0.092, both of them have air cavities on their bottoms, but Model C2.2 has more air cavities compared to Model C2. Therefore, due to the difference in the water cavity, the wetted surface area for each variation of step position became different. The differences in the wetted area contours are explained in Figure 22.

In Fig. 22, the differences in contour for the volume fraction of water values are explained, which indicate the differences in wetted surface area. The wetted surface area is also calculated including the spray that occurs. At low velocity, Fr_∇ = 3.72±1.3%, it can be observed that Model C2.4 has the smallest wetted surface area. Meanwhile, at high velocity, Fr_∇ = 6.02±2.1%, it can be seen that Model C2.2 has a smaller wetted surface area. It can also be observed that Model C2 has the highest wetted surface area both at low and high velocities. Therefore, it can be concluded that the position of these two steps greatly influences the wetted surface area values at each velocity.

In Fig. 23, a comparison of the wave-making elevation contours of the C2 and C2.2 models is presented. It can be observed that the angle of the Kelvin wave generated from the C2 model was slightly larger than that of the C2.2 model. This result indicated that the wave resistance of the C2 model was higher than that of the C2.2 model. High wave resistance occurred due to significant pressure contour differences on the boat's hull. The pronounced pressure contours mean that there was a sudden change in pressure from very high to very low, which caused a high wave elevation. This extreme pressure difference led to the formation of high wave-making elevation contours. This phenomenon can be observed in Fig. 24 as the pressure coefficient distribution in the total and static pressure. Equation (24) describes the total pressure coefficient and Equation (25) describes the dynamic pressure coefficient, where: p is local pressure; ρ_i is density of fluids that consist of water and air; V is velocity of the boat. In Fig. 25 and Fig. 26, the local pressure curve showed that the C2 model had a pattern that went up and down, and then up again. This was different from the C2.2 model, where when the pressure value increased and then decreased, the decrease was not as extreme as in the C2 model. The distance between the steps also resulted in a significant difference in pressure contours, as exemplified by the C2 model, which had the longest distance between steps compared to the other models. Furthermore, the differences in wetted length, wetted surface area, and displacement due to different lift forces can also cause differences in wave-making resistance:

$$c_{p_{(\text{total})}} = \frac{p_{(\text{total})}}{0.5\rho_i V^2} \tag{24}$$

$$c_{p\,(dynamic)} = \frac{p_{(total)} - p_{(static)}}{0.5\rho_i V^2} \quad (25)$$

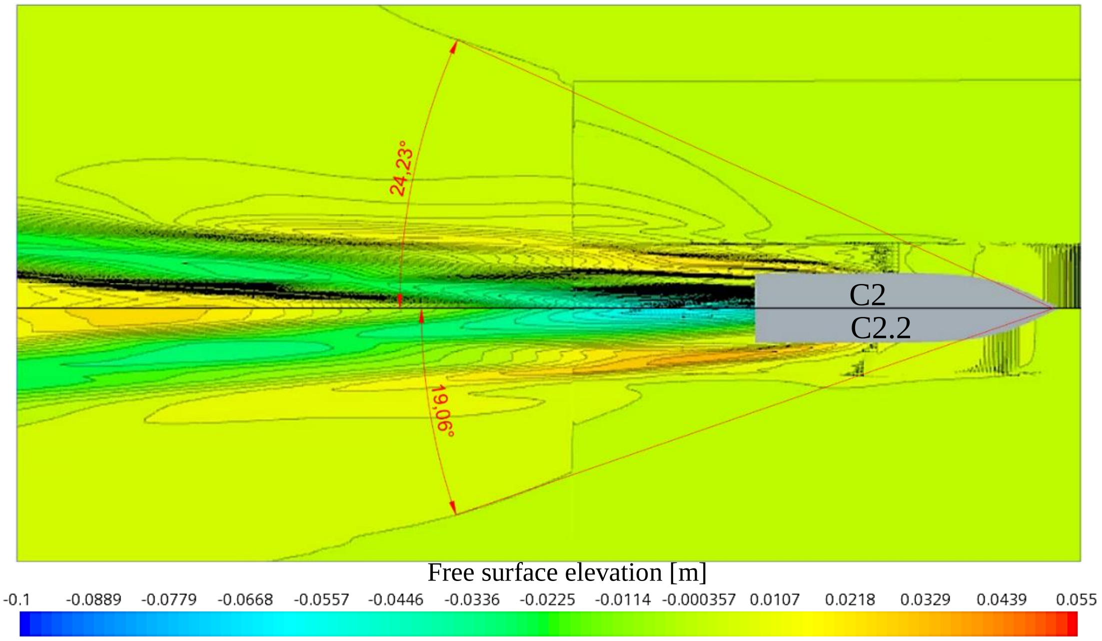

Fig. 23 Comparison of wave-making elevation distribution for C2 and C2.2 models at 10.13 m/s (Fr_∇ = 6.01)

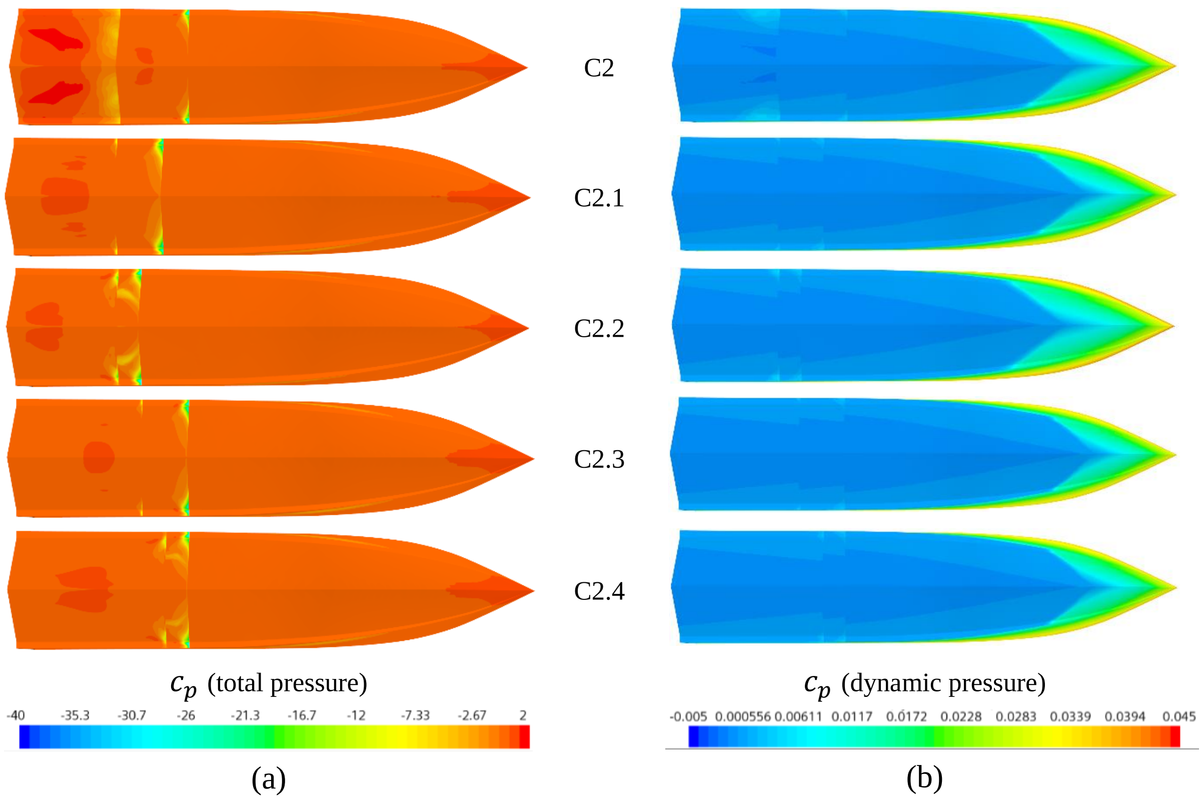

Fig. 24 Comparison of pressure coefficients (c_p) distribution: (a) total pressure and (b) dynamic pressure of all models at 10.13 m/s (Fr_∇ = 6.01)

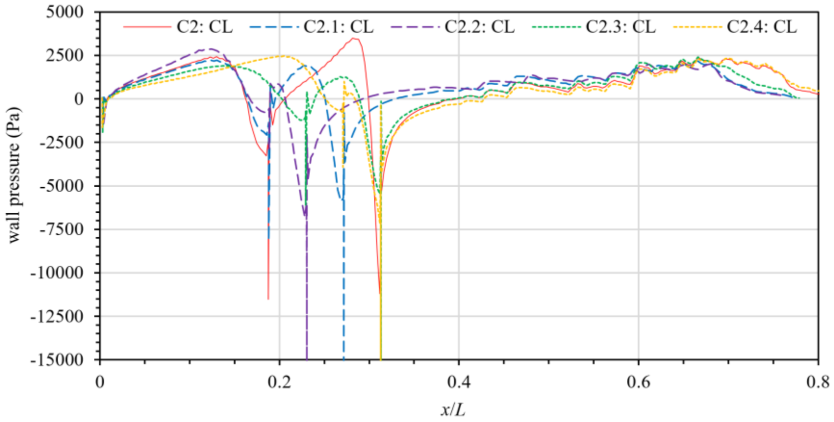

Fig. 25 Comparison of local wall pressure values of each model on the centerline

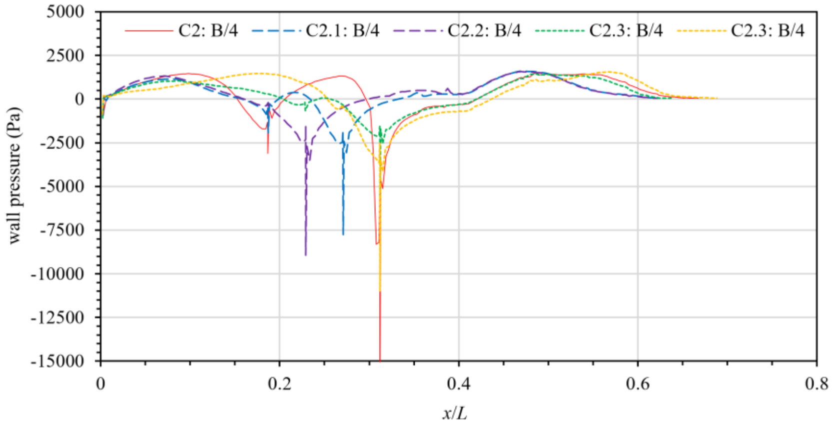

Fig. 26 Comparison of local wall pressure values of each model on the ¼ Beam

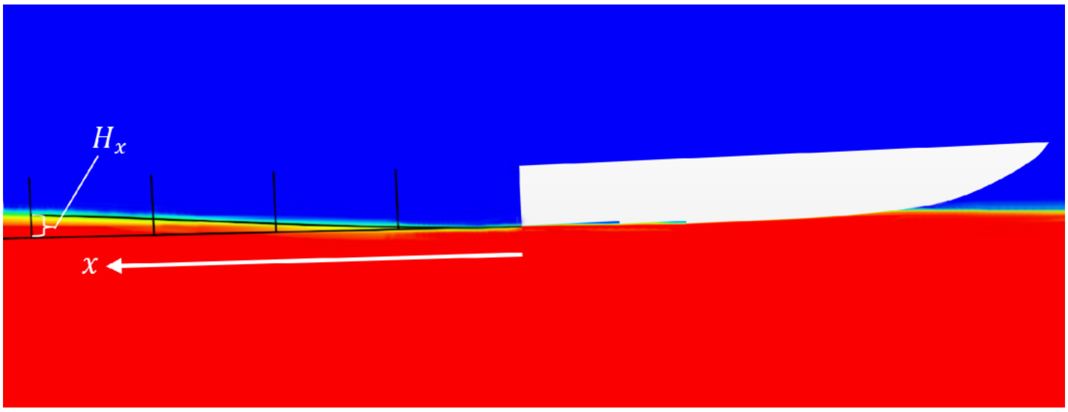

Fig. 27 The wake profile calculation is based on the method proposed by Savitsky and Morabito [69]

The performance of planing vessels, both conventional and with steps, can be analyzed based on the wake profile created at the stern of the hull [69]. The wake profile is illustrated in Fig. 27. By using several models and speeds, wake profile plots were obtained as shown in Fig. 28. On the horizontal axis, denoted as x/B, where x is the distance compared to the hull beam as indicated in Fig. 27. On the vertical axis, denoted as H_x/H_s, where H_x is the wake profile height at distance x compared to the step height as shown in Fig. 27. From the results of these plots, it can be observed that as the Froude number (Fr_∇) or vessel speed increases, the wake profile becomes lower. This indicates that resistance increases with lower wake profile height, and vice versa for lower resistance where the wake profile height becomes higher.

From the wake profile plots at the same speed, it was observed that model C2.2 consistently has the highest wake profile, while model C2.4 consistently has the lowest wake profile. Further analysis on this inconsistency with the resistance results needs to be investigated in future research. The resistance results show that at Fr_∇ = 3.72, the order of resistance values is C2 > C2.2 > C2.4, and at Fr_∇ = 6.01, the order of resistance is C2 > C2.4 > C2.2.

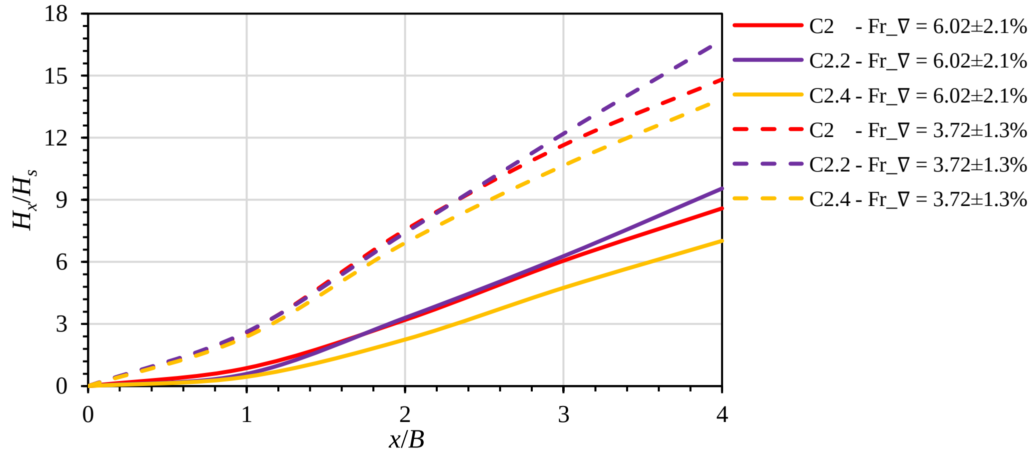

Fig. 28 The results of the comparison of the height of the wake profile of several models and the speed.

3.6 Dynamic trim results

This subsection describes the analysis of the dynamic trim results from CFD simulation. Overall, the graph of Fig. 29 organized the outcomes of the dynamic trim of all model modifications. Fig. 30 and Fig. 31 provides an analysis of how the positions of the first and second steps affect the results of the dynamic trim.

The outcomes of the dynamic trim for all model variations on the Fr_∇ value are shown in Fig. 29. All dynamic trim results demonstrated that the trim decreased as boat speed (or Fr_∇) increased. Increased trim occurred when the first step was shifted backward, as shown in models C2.2 and C2.1 compared to model C2. According to models C2.4 and C2.3, moving the second step forward results in a lower trim value.

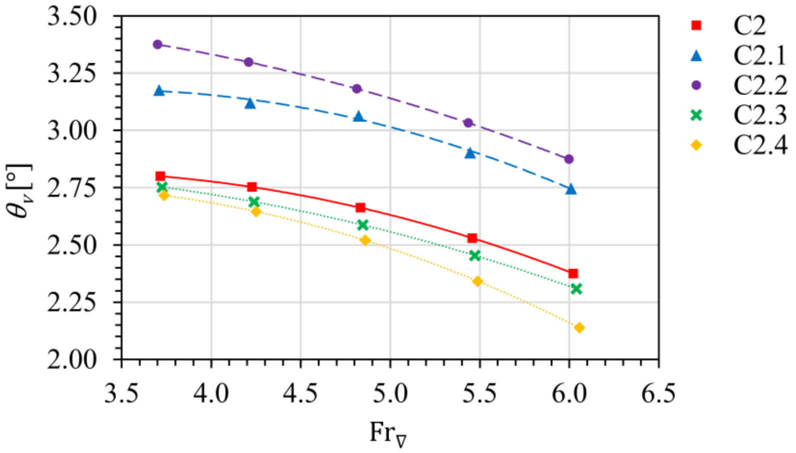

Fig. 29 Dynamic trim results for all model variations

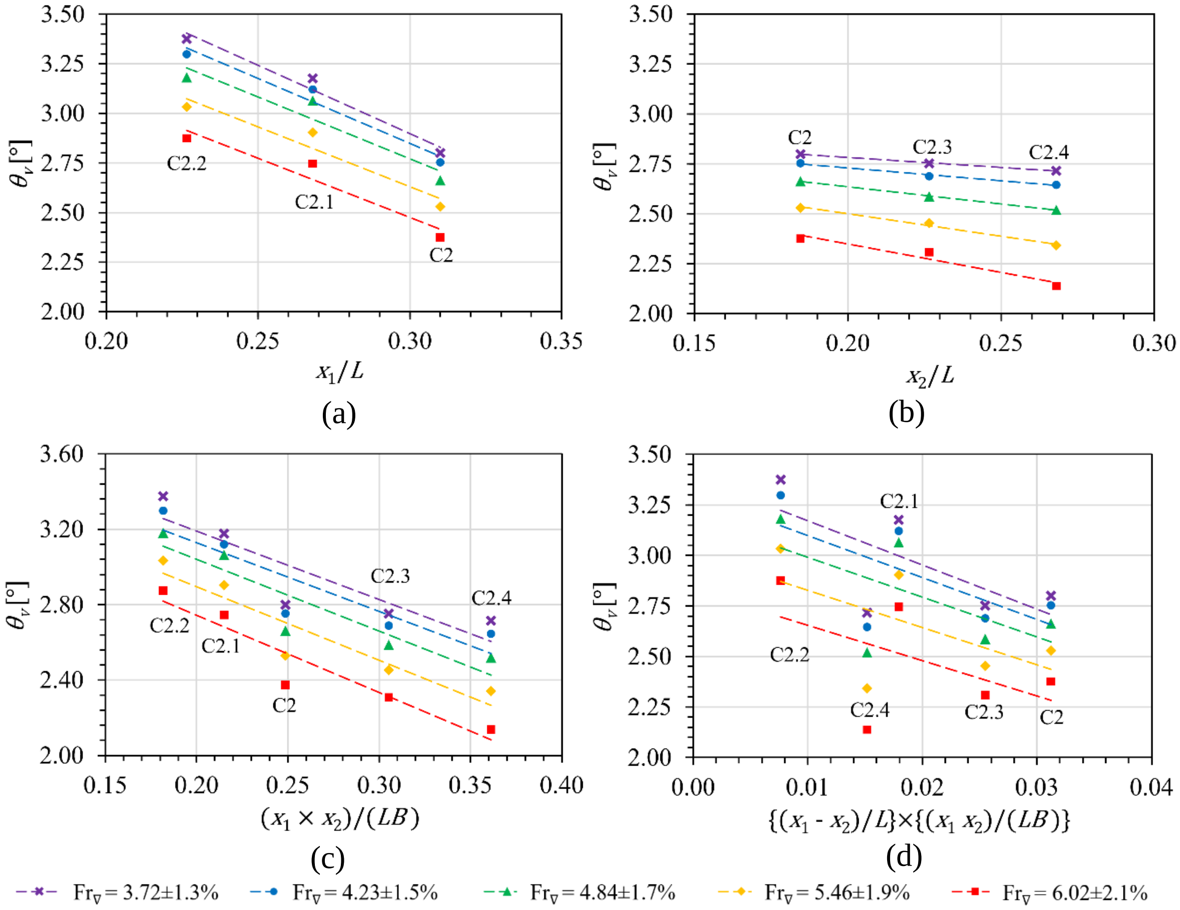

Fig. 30 The graphs plot the dynamic trim against the position of the hull steps: (a) first step only, (b) second step only, (c) the multiplication of the two steps, and (d) the difference between the two steps times the multiplication of the two steps

Fig. 30 explains how the position of the two steps affected the outcomes of the dynamic trim. The dynamic trim decreased as the first step was moved farther ahead, as seen in Fig. 30 (a), but the dynamic trim decreases a bit as the second step was moved farther forward, as seen in Fig. 30 (b). The graph in Fig. 30 (c) demonstrated that the lower dynamic trim was produced due to the higher multiplying positions of the two steps. It will also be the same in the graph showing how the dynamic trim depicted in Fig. 30 (d) was affected by the distance between two steps multiplied by the multiplication of the two steps. This result was in line with what was found by Najafi et al. [71,72], where shifting the step hull position closer to the transom can increase the dynamic trim value. The trim values of these models can be observed from the distribution of wall pressure in Fig. 24 to Fig. 26. It can be seen that models C2.2 and C2.1 had a pressure distribution area that appeared to be more towards the rear than the other models. This event was the cause of the higher trim values of Model C2.2 and Model C2.1.

The author also attempted to find the relationship between the position of the two steps, distance between the steps, and boat speed parameters to the dynamic trim results, which was then obtained and explained in Fig. 31. The curve shows the relationship of the three variations that had been made. The distance between the two steps was represented by $x_1 - x_2$, and the position of the both steps was represented by the multiplication of x_1 and x_2. All parameters were made into nondimensional form. The regression results showed a satisfactory value, with a determination coefficient of R^2 = 0.9371 and a slope of -0.7032.

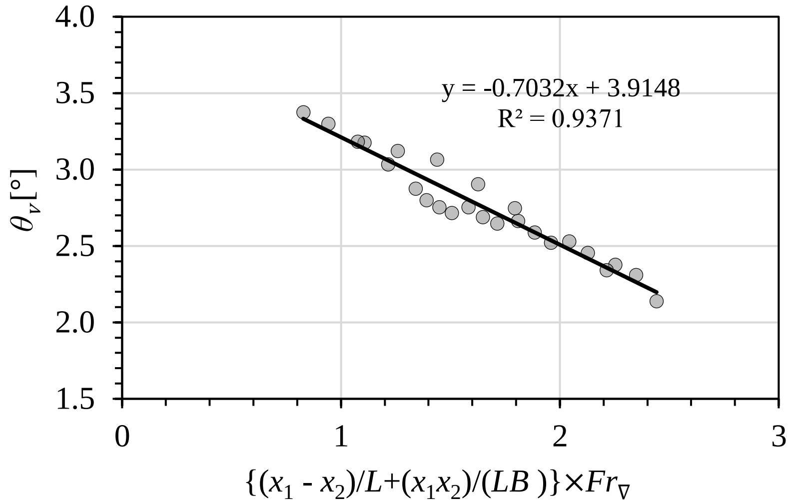

Fig. 31 Regression analysis of the relationship between the distance and the location of the double step, as well as the speed parameters to the dynamic trim result

3.7 Dynamic sinkage results

The analysis of the findings of dynamic sinkage is covered in this subsection. The outcomes of the dynamic sinkage of all model variations were organized in the graph of Fig. 32. A breakdown of how the first and second step positions impact the dynamic sinkage outcomes is shown in Fig. 33 and Fig. 34.

Fig. 32 shows the results of the dynamic sinkage for all model variations on the Fr_∇ value. The sinkage increased as the boat's speed (or Fr_∇) increased, as shown by all dynamic sinkage data. As demonstrated in models C2.2 and C2.1 compared to model C2, increased sinkage happened when the first step was moved backward. When the second step was shifted forward, as in models C2.4 and C2.3, it produced dynamic sinkage values that were relatively unchanged from model C2.

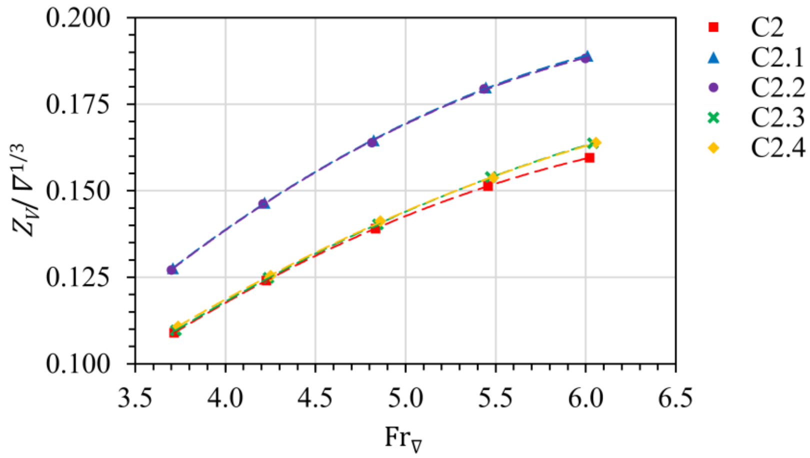

Fig. 32 Dynamic sinkage results for all model variations

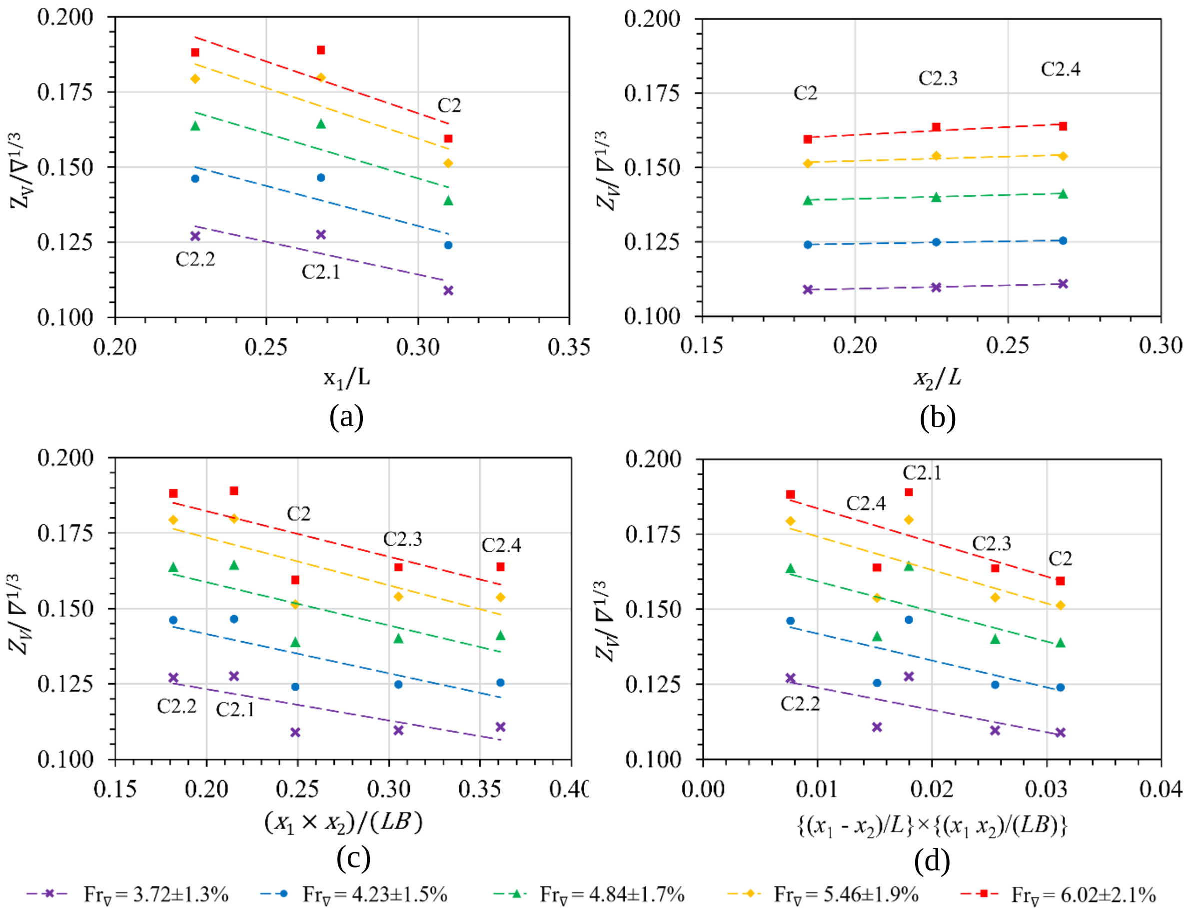

Fig. 33 The graphs plot the dynamic sinkage against the position of the hull steps: (a) first step only, (b) second step only, (c) the multiplication of the two steps, and (d) the difference between the two steps times the multiplication of the two steps

Fig. 33 illustrates how the positioning of the two steps impacted the outcomes of the dynamic sinkage. Fig. 33 (a) shows how the dynamic sinkage decrease as the first step was shifted forward. Meanwhile, Fig. 33 (b) shows how the effect of shifting the second step forward did not really have an impact on the dynamic sinkage value. The graph in Fig. 33 (c) illustrates that the higher multiplication of the two-step positions resulted in lower dynamic sinkage. The graph illustrating the impact of the distance between two steps multiplied by the multiplication of the two steps will decrease the dynamic sinkage results, as shown in Fig. 33 (d). This outcome is consistent with what Najafi et al. [71,72] discovered: moving the stepped hull closer to the transom can raise the dynamic sinkage value.

The author also tried to establish a correlation between three parameters, namely the position and distance between two steps and the boat's speed, with the dynamic sinkage outcomes presented in Fig. 34. The plot illustrates the relationship between these three varied variables. The distance between the steps was denoted by $x_1 - x_2$, while the position of both steps was obtained by multiplying x_1 and x_2. To standardize the values, all parameters were transformed into nondimensional form. The regression analysis yielded a weak correlation, with a determination coefficient of R^2 = 0.0109 and a slope of 0.0109.

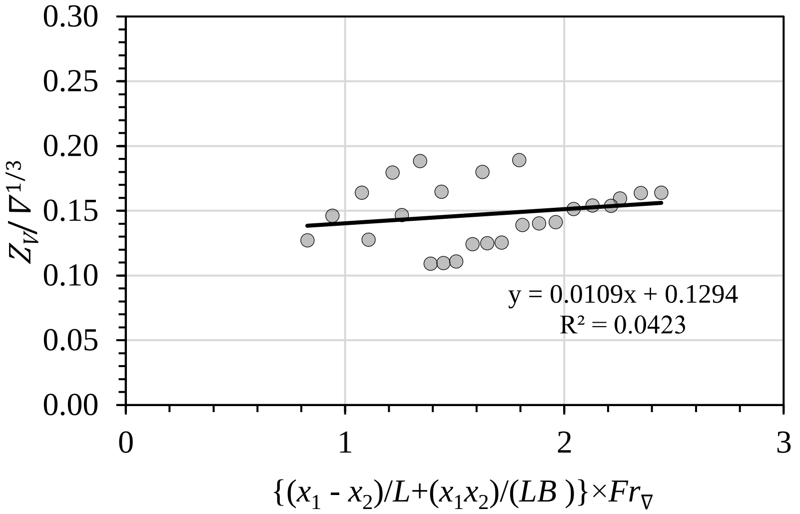

Fig. 34 Regression analysis of the relationship between the distance and the location of the double step, as well as the speed parameters to the dynamic sinkage result

4. Conclusion

CFD simulation has been performed to analyze the effect of the position of the first and second steps on the double-stepped planing hull performance. The modified position of the steps came from the hull taken from the literature, and the hull model was validated. The results analyzed were resistance, dynamic trim, and dynamic sinkage. CFD simulation settings used the multi fluids, unsteady RANS equations, and dynamic overset mesh methods.

The positions of the two steps were formulated in the form of a non-dimensional equation and had a relationship to the results sought: namely the total resistance (R_T), dynamic trim (θ_V), and dynamic sinkage (Z_V). The equation is: $\{(x_1 - x_2)/L + (x_1x_2)/(LB)\} \times Fr_\nabla$. Where: x_1 is the distance of the front step from the transom; x_2 is the rear step distance from the transom; L is the length of the boat; B is the beam of the boat; Fr_∇ is the volume Froude number. The two step positions were judged to be backwards or forwards which can be seen in the multiplication value of x_1 and x_2. The distance between the two steps can be assessed by $x_1 - x_2$. The speed of the boat can be assessed by the Froude number. The relationship of these parameters to the results can be seen in Fig. 13, Fig. 31, and Fig. 34.

The position of the two steps clearly affected the boat's performance. The analysis results of the position of the steps on the resistance showed that shifting the first step further forward caused the resistance to increase. Meanwhile, moving the second step further caused the resistance to decrease slightly. Moving both steps (the first and second) further forward caused resistance to decrease at low speeds but increase at high speeds. The longer distance between the first and second steps caused the resistance to increase. According to the analysis of how the position of the steps affected the dynamic trim, moving the first step forward reduced the dynamic trim. However, the dynamic trim got a bit higher as the second step moved forward. The dynamic trim was reduced when moving both the first and second steps further forward. The dynamic trim decreased as the distance between the first and second steps are longer. The dynamic sinkage was shown to be reduced when the first step was moved further forward. Still, changing the position of the second step did not change the dynamic sinkage. The dynamic sinkage was decreased by shifting both the first and second steps forward. The dynamic sinkage reduced as the distance between the first and second steps is longer.

Because there are several weaknesses in the results of this study, it is necessary to improve the research to strengthen the findings. The first weakness lies in the validation test, which yielded unsatisfactory experimental results. The next weakness is the absence of a comprehensive measurement of the wake profile of the two steps, similar to what was conducted by Savitsky and Morabito [69]. To gain a complete global perspective, future investigations should consider more sophisticated modeling techniques, conduct extensive parametric analyses, and optimize studies with additional parameters. More parameters include step height (Hs), L/B ratio, deadrise angel (β), more velocities or Froude number, and others.

ACKNOWLEDGMENTS

This research was supported by the Hydrodynamics laboratory of the Department of Naval Architecture, Faculty of Engineering, Universitas Diponegoro.

REFERENCES

[1] Doctors, L.J., 1985. Hydrodynamics of High-speed Small Craft. Department of Naval Engineering and Marine Engineering, The University of Michigan, Michigan.

[2] Buhaug, Ø., Corbett, J., Endresen, Ø., Eyring, V., Faber, J., Hanayama, S., Lee, D.., Lee, D., Lindstad, H., Markowska, A., Mjelde, A., Nelissen, D., Nilsen, J., Pålsson, C., Winebrake, J., Wu, W., Yoshida, K., 2009. Second IMO GHG Study2009. International Maritime Organization (IMO). https://doi.org/10.1163/187529988X00184

[3] Smith, T.W.P., Jalkanen, J.P., Anderson, B.A., Corbett, J.J., Faber, J., Hanayama, S., O'Keeffe, E., Parker, S., Johansson, L., Aldous, L., Raucci, C., Traut, M., Ettinger, S., Nelissen, D., Lee, D.S., Ng, S., Agrawal, A., Winebrake, J.J. et al., 2014. Third IMO GHG Study 2014. International Maritime Organization (IMO) London, UK. https://doi.org/10.1017/CBO9781107415324.004

[4] ICCT, 2011. Reducing Greenhouse Gas Emissions from Ships. *White Paper*, (11).

[5] Molland, A.F., Turnock, S.R., Hudson, D.A., Utama, I.K.A.P., 2014. Reducing ship emissions: A review of potential practical improvements in the propulsive efficiency of future ships. *Transactions of the Royal Institution of Naval Architects Part A: International Journal of Maritime Engineering*, 156(PART A2), 175–88. https://doi.org/10.3940/rina.ijme.2014.a2.289

[6] Onwuegbuchunam, D.E., Ogbenna, F.C., Ezeanya, N.C., Okeke, K.O., 2019. Ship Hull Form Optimization: A Computational Fluid Dynamics (CFD) Approach. *International Journal of Transportation Engineering and Technology*, 5(3), 43. https://doi.org/10.11648/j.ijtet.20190503.11

[7] Kleinsorge, E., Lindner, H., Wagner, J., Bronsart, R., 2016. Ship hull form optimization using scenario methods. *PRADS 2016 - Proceedings of the 13th International Symposium on PRActical Design of Ships and Other Floating Structures*, 4-8 September, Copenhagen, Denmark.

[8] Hakim, M.L., Tuswan, T., Firdaus, A., Mursid, O., 2023. Investigating the Comparison of Ship Resistance Components between U and V-Shaped Hulls. *Jurnal Teknologi*, 85(3), 153–64. https://doi.org/10.11113/jurnalteknologi.v85.19382

[9] Zhao, C., Wang, W., Jia, P., Xie, Y., 2021. Optimisation of Hull Form of Ocean-Going Trawler. *Brodogradnja*, 72(4), 33–46. https://doi.org/10.21278/brod72403

[10] Zis, T.P.V., Psaraftis, H.N., Ding, L., 2020. Ship weather routing: A taxonomy and survey. *Ocean Engineering*, 213, 107697. https://doi.org/10.1016/j.oceaneng.2020.107697

[11] Taskar, B., Andersen, P., 2020. Benefit of speed reduction for ships in different weather conditions. *Transportation Research Part D: Transport and Environment*, 85, 102337. https://doi.org/10.1016/j.trd.2020.102337

[12] Hakim, M.L., Nugroho, B., Suastika, I.K., Utama, I.K.A.P., 2021. Alternative Empirical Formula for Predicting the Frictional Drag Penalty due to Fouling on the Ship Hull using the Design of Experiments (DOE) Method. *International Journal of Technology*, 12(4), 829. https://doi.org/10.14716/ijtech.v12i4.4692

[13] Hakim, M.L., Suastika, I.K., Utama, I.K.A.P., 2023. A practical empirical formula for the calculation of ship added friction-resistance due to (bio)fouling. *Ocean Engineering*, 271, 113744. https://doi.org/10.1016/j.oceaneng.2023.113744

[14] Hakim, M.L., Maqbulyani, N., Nugroho, B., Suastika, I.K., Utama, I.K.A.P., 2021. Wind-Tunnel Experiments and CFD Simulations to Study the Increase in Ship Resistance Components due to Roughness. *Journal of Sustainability Science and Management*, 16(3), 144–63.

https://doi.org/10.46754/jssm.2021.04.012

[15] Schultz, M.P., Bendick, J.A., Holm, E.R., Hertel, W.M., 2011. Economic impact of biofouling on a naval surface ship. *Biofouling*, 27(1), 87–98. https://doi.org/10.1080/08927014.2010.542809

[16] Degiuli, N., Farkas, A., Martić, I., Grlj, C.G., 2023. Optimization of Maintenance Schedule for Containerships Sailing in the Adriatic Sea. *Journal of Marine Science and Engineering*, 11(1), 201. https://doi.org/10.3390/jmse11010201

[17] Farkas, A., Degiuli, N., Martić, I., 2021. Assessment of the effect of biofilm on the ship hydrodynamic performance by performance prediction method. *International Journal of Naval Architecture and Ocean Engineering*, 13, 102–14. https://doi.org/10.1016/j.ijnaoe.2020.12.005

[18] Dinariyana, A., Deva, P.P., Ariana, I.M., 2022. Development of Model-Driven Decision Support System to Scheduling Underwater Hull Cleaning. *Brodogradnja*, 73(3), 21–37. https://doi.org/10.21278/brod73302

[19] Monty, J.P., Dogan, E., Hanson, R., Scardino, A.J., Ganapathisubramani, B., Hutchins, N., 2016. An assessment of the ship drag penalty arising from light calcareous tubeworm fouling. *Biofouling*, 32(4), 451–64. https://doi.org/10.1080/08927014.2016.1148140

[20] Song, S., Demirel, Y.K., Atlar, M., 2019. An investigation into the effect of biofouling on the ship hydrodynamic characteristics using CFD. *Ocean Engineering*, 175, 122–37. https://doi.org/10.1016/j.oceaneng.2019.01.056

[21] Suastika, I.K., Hakim, M.L., Nugroho, B., Nasirudin, A., Utama, I.K.A.P., Monty, J.P., Ganapathisubramani, B., 2021. Characteristics of drag due to streamwise inhomogeneous roughness. *Ocean Engineering*, 223, 108632. https://doi.org/10.1016/j.oceaneng.2021.108632

[22] Hakim, M.L., Nugroho, B., Chin, R.C., Putranto, T., Suastika, I.K., Utama, I.K.A.P., 2020. Drag penalty causing from the roughness of recently cleaned and painted ship hull using RANS CFD. *CFD Letters*, 12(3), 78–88. https://doi.org/10.37934/cfdl.12.3.7888

[23] Farkas, A., Degiuli, N., Martić, I., Vujanović, M., 2021. Greenhouse gas emissions reduction potential by using antifouling coatings in a maritime transport industry. *Journal of Cleaner Production*,. https://doi.org/10.1016/j.jclepro.2021.126428

[24] Yeginbayeva, I.A., Atlar, M., 2018. An experimental investigation into the surface and hydrodynamic characteristics of marine coatings with mimicked hull roughness ranges. *Biofouling*, 34(9), 1001–19. https://doi.org/10.1080/08927014.2018.1529760

[25] Schultz, M.P., 2004. Frictional Resistance of Antifouling Coating Systems. *Journal of Fluids Engineering*, 126(6), 1039–47. https://doi.org/10.1115/1.1845552

[26] Atencio, B.N., Chernoray, V., 2019. A resolved RANS CFD approach for drag characterization of antifouling paints. *Ocean Engineering*, 171, 519–32. https://doi.org/10.1016/j.oceaneng.2018.11.022

[27] Schultz, M.P., 2007. Effects of coating roughness and biofouling on ship resistance and powering. *Biofouling*, 23(5), 331–41. https://doi.org/10.1080/08927010701461974

[28] Felayati, F.M., Semin, S., Cahyono, B., Bakar, R.A., 2021. Numerical Investigation of Dual-Fuel Engine Improvements Using Split Injection Natural Gas Coupled with Diesel Injection Timings at Low Load Condition. *International Journal on Engineering Applications (IREA)*, 9(1), 31. https://doi.org/10.15866/irea.v9i1.19622

[29] Felayati, F.M., Semin, Cahyono, B., Prayogi, U., Winarno, A., 2022. Future perspective of the ship alternative fuels in Indonesia. *IOP Conference Series: Earth and Environmental Science*, 972(1), 012024. https://doi.org/10.1088/1755-1315/972/1/012024

[30] Nasirudin, A., Hasanudin, H., Utama, D., Tahwoto, L.P., 2020. Determination of PV Power and Battery Capacity Size for a Leisure Solar Powered Boat at Kalimas River, Surabaya, Indonesia. *Kapal: Jurnal Ilmu Pengetahuan Dan Teknologi Kelautan*, 17(3), 123–9. https://doi.org/10.14710/kapal.v17i3.31965

[31] Sultoni, A.I., Ali, M.M., Aji, Z.P., 2020. Hybrid Propulsion System (PV / Gasoline) For Small Fishing Vessels. *Kapal: Jurnal Ilmu Pengetahuan Dan Teknologi Kelautan*, 17(1), 1–6. https://doi.org/10.14710/kapal.v17i1.25613

[32] Tuswan, T., Sari, D.P., Muttaqie, T., Prabowo, A.R., Soetardjo, M., Murwantono, T.T.P., Utina, R., Yuniati, Y., 2023. Representative application of LNG-fuelled ships: a critical overview on potential ghg emission reductions and economic benefits. *Brodogradnja*, 74(1), 63–83. https://doi.org/10.21278/brod74104

[33] Abar, I.A.C., Utama, I.K.A.P., 2019. Effect of the Incline Angle of Propeller Boss Cap Fins (PBCF) on Ship Propeller Performance. *International Journal of Technology*, 10(5), 1056.

https://doi.org/10.14716/ijtech.v10i5.2256

[34] Arifin, M.D., Felayati, F.M., Muhammad, A.H., 2022. Flow Separation Evaluation on Tubercle Ship Propeller. *CFD Letters*, 14(4), 43–50. https://doi.org/10.37934/cfdl.14.4.4350

[35] Hakim, M.L., Nugroho, B., Nurrohman, M.N., Suastika, I.K., Utama, I.K.A.P., 2019. Investigation of fuel consumption on an operating ship due to biofouling growth, quality of anti-fouling coating. *IOP Conference Series: Earth and Environmental Science*, 339(1), 012037. https://doi.org/10.1088/1755-1315/339/1/012037

[36] Tian, L., Yin, Y., Bing, W., Jin, E., 2021. Antifouling Technology Trends in Marine Environmental Protection. *Journal of Bionic Engineering*, 18(2), 239–63. https://doi.org/10.1007/s42235-021-0017-z

[37] Grigson, C., 1992. Drag Losses of New Ships Caused by Hull Finish. *Journal of Ship Research*, 36(02), 182–96. https://doi.org/10.5957/jsr.1992.36.2.182

[38] Verma, S., Mohanty, S., Nayak, S.K., 2019. A review on protective polymeric coatings for marine applications. *Journal of Coatings Technology and Research*, 16(2), 307–38. https://doi.org/10.1007/s11998-018-00174-2

[39] Dafforn, K.A., Lewis, J.A., Johnston, E.L., 2011. Antifouling strategies: History and regulation, ecological impacts and mitigation. *Marine Pollution Bulletin*, 62(3), 453–65. https://doi.org/10.1016/j.marpolbul.2011.01.012

[40] Khanna, A.S., Kasturi, V., Grover, P., 2017. Development of Superfine Nano-Composites Antifouling Coatings for Ship Hulls. *Ceramic Transactions*, 263, 425-442. https://doi.org/10.1002/9781119407270.ch40

[41] Yebra, D.M., Kiil, S., Dam-Johansen, K., 2004. Antifouling technology—past, present and future steps towards efficient and environmentally friendly antifouling coatings. *Progress in Organic Coatings*, 50(2), 75–104. https://doi.org/10.1016/j.porgcoat.2003.06.001

[42] Sasaki, N., Atlar, M., Kuribayashi, S., 2016. Advantages of twin rudder system with asymmetric wing section aside a propeller. *Journal of Marine Science and Technology*, 21(2), 297–308. https://doi.org/10.1007/s00773-015-0352-z

[43] Koushan, K., Krasilnikov, V., Nataletti, M., Sileo, L., Spence, S., 2020. Experimental and Numerical Study of Pre-Swirl Stators PSS. *Journal of Marine Science and Engineering*, 8(1), 47. https://doi.org/10.3390/jmse8010047

[44] Bakica, A., Vladimir, N., Gatin, I., Jasak, H., 2020. CFD simulation of loadings on circular duct in calm water and waves. *Ships and Offshore Structures*, 15(sup1), S110–22. https://doi.org/10.1080/17445302.2020.1730082

[45] Gaggero, S., Martinelli, M., 2022. Pre- and post-swirl fins design for improved propulsive performances. *Ship Technology Research*, 69(1), 31–49. https://doi.org/10.1080/09377255.2021.1934362

[46] Savitsky, D., 1992. Overview of planning hull developments. *High-Performance Marine Vehicle Conference*, American Society of Naval Engineers, Alexandria. p. PC1–14.

[47] Faltinsen, O.M., 2006. Hydrodynamics of High-Speed Marine Vehicles [Internet]. Hydrodynamics of High-Speed Marine Vehicles. Cambridge University Press. https://doi.org/10.1017/CBO9780511546068

[48] Molland, A.F., Turnock, S.R., Hudson, D.A., 2017. Ship Resistance and Propulsion [Internet]. Ship Resistance and Propulsion. Cambridge University Press, Cambridge. https://doi.org/10.1017/9781316494196

[49] Avci, A.G., Barlas, B., 2019. An experimental investigation of interceptors for a high speed hull. *International Journal of Naval Architecture and Ocean Engineering*, 11(1), 256–73. https://doi.org/10.1016/j.ijnaoe.2018.05.001

[50] Mansoori, M., Fernandes, A.C., 2017. Interceptor and trim tab combination to prevent interceptor's unfit effects. *Ocean Engineering*, 134, 140–56. https://doi.org/10.1016/j.oceaneng.2017.02.024

[51] Samuel, S., Mursid, O., Yulianti, S., Kiryanto, Iqbal, M., 2022. Evaluation of Interceptor Design to Reduce Drag on Planing Hull. *Brodogradnja*, 73(3), 93–110. https://doi.org/10.21278/brod73306

[52] Sahin, O.S., Kahramanoglu, E., Cakici, F., 2022. Numerical evaluation on the effects of interceptor layout and blade heights for a prismatic planing hull. *Applied Ocean Research*, 127, 103302. https://doi.org/10.1016/j.apor.2022.103302

[53] Park, J.-Y., Choi, H., Lee, J., Choi, H., Woo, J., Kim, S., Kim, D.J., Kim, S.Y., Kim, N., 2019. An experimental study on vertical motion control of a high-speed planing vessel using a controllable interceptor in waves. *Ocean Engineering*, 173, 841–50. https://doi.org/10.1016/j.oceaneng.2019.01.019

[54] Rijkens, A.A.K., Keuning, J.A., Huijsmans, R.H.M., 2011. A computational tool for the design of ride control systems for fast planing vessels. *International Shipbuilding Progress*, 58, 165–90. https://doi.org/10.3233/ISP-2012-0074

[55] Utomo, B., Samuel, S., Yulianti, S., Rindo, G., Iqbal, M., Fathuddiin, A., 2022. CFD Simulation Verification Processes at Planing Hulls using An Interceptor. *Kapal: Journal of Marine Science and Technology*, 19(3), 141–50. https://doi.org/10.14710/kapal.v19i3.48319

[56] Suneela, J., Sahoo, P., 2021. Numerical Investigation of Interceptor Effect on Sea Keeping Behavior of Planing Hull Advancing in Regular Head Waves. *Brodogradnja*, 72(2), 73–92. https://doi.org/10.21278/brod72205

[57] Mansoori, M., Fernandes, A.C., 2016. The interceptor hydrodynamic analysis for controlling the porpoising instability in high speed crafts. *Applied Ocean Research*, 57, 40–51. https://doi.org/10.1016/j.apor.2016.02.006

[58] Ertogan, M., Wilson, P.A., Tayyar, G.T., Ertugrul, S., 2017. Optimal trim control of a high-speed craft by trim tabs/interceptors Part I: Pitch and surge coupled dynamic modelling using sea trial data. *Ocean Engineering*, 130, 300–9. https://doi.org/10.1016/j.oceaneng.2016.12.007

[59] Budiarto, U., Samuel, S., Wijaya, A.A., Yulianti, S., Kiryanto, K., Iqbal, I., 2022. Stern Flap Application on Planing Hulls to Improve Resistance. *International Journal of Engineering, Transaction C: Aspects*, 35(12). https://doi.org/10.5829/IJE.2022.35.12C.06

[60] Ghadimi, P., Loni, A., Nowruzi, H., Dashtimanesh, A., Tavakoli, S., 2014. Parametric Study of the Effects of Trim Tabs on Running Trim and Resistance of Planing Hulls. *Advanced Shipping and Ocean Engineering*, 3(1), 1–12.

[61] Fitriadhy, A., Pheng, L.Y., Adzkh, I.N.H., Mahmuddin, F., Bakar, A.A., Musa, M.A., Sulaiman, M.S., 2022. Computational Investigation of Pitch Motion of a High-Speed Craft Incorporated with Trim-Tabs. *CFD Letters*, 14(6), 56–71. https://doi.org/10.37934/cfdl.14.6.5671

[62] Suastika, K., Hidayat, A., Riyadi, S., 2017. Effects of the Application of a Stern Foil on Ship Resistance: A Case Study of an Orela Crew Boat. *International Journal of Technology*, 8(7), 1266. https://doi.org/10.14716/ijtech.v8i7.691

[63] Budiyanto, M.A., Syahrudin, M.F., Murdianto, M.A., 2020. Investigation of the effectiveness of a stern foil on a patrol boat by experiment and simulation. Pham D, editor. *Cogent Engineering*, 7(1), 1716925. https://doi.org/10.1080/23311916.2020.1716925

[64] Syahrudin, M.F., Budiyanto, M.A., Murdianto, M.A., 2020. Analysis of the Use of Stern Foil on the High Speed Patrol Boat on Full Draft Condition. *Evergreen*, 7(2), 262–7. https://doi.org/10.5109/4055230

[65] Budiyanto, M.A., Murdianto, M.A., Syahrudin, M.F., 2020. Study on the resistance reduction on high-speed vessel by application of stern foil using CFD simulation. *CFD Letters*, 12(4), 35-42. https://doi.org/10.37934/cfdl.12.4.3542

[66] Dwiputera, H., Prawira, N.Y., Budiyanto, M.A., Arif, M., 2020. Effect of Angle of Attack Variation of Stern Foil on High-Speed Craft on Various Speed with Computational Fluid Dynamics Method. *International Journal of Technology*, 11(7), 1359-1369. https://doi.org/10.14716/ijtech.v11i7.4467

[67] Taunton, D.J., Hudson, D.A., Shenoi, R.A., 2010. Characteristics of A series of high speed hard chine planing hulls - Part 1: Performance in calm water. *Transactions of the Royal Institution of Naval Architects Part B: International Journal of Small Craft Technology*, 152, 55–75.

[68] Roshan, F., Dashtimanesh, A., Bilandi, R.N., 2020. Hydrodynamic Characteristics of Tunneled Planing Hulls in Calm Water. *Brodogradnja*, 71(1), 19–38. https://doi.org/10.21278/brod71102

[69] Savistky, D., Morabito, M., 2010. Surface Wave Contours Associated with the Forebody Wake of Stepped Planing Hulls. *Marine Technology and SNAME News*, 47(01), 1–16. https://doi.org/10.5957/mtsn.2010.47.1.1

[70] Vitiello, L., Mancini, S., Bilandi, R.N., Dashtimanesh, A., De Luca, F., Nappo, V., 2022. A comprehensive stepped planing hull systematic series: Part 1 - Resistance test. *Ocean Engineering*, 266, 112242. https://doi.org/10.1016/j.oceaneng.2022.112242

[71] Najafi, A., Nowruzi, H., Ameri, M.J., 2020. Hydrodynamic Assessment of Stepped Planing Hulls Using Experiments. *Ocean Engineering*, Elsevier Ltd. 217(424), 107939. https://doi.org/10.1016/j.oceaneng.2020.107939

[72] Najafi, A., Nowruzi, H., Karami, M., Javanmardi, H., 2019. Experimental investigation of the wetted surfaces of stepped planing hulls. *Ocean Engineering*, 187, 106164. https://doi.org/10.1016/j.oceaneng.2019.106164

[73] De Marco, A., Mancini, S., Miranda, S., Scognamiglio, R., Vitiello, L., 2017. Experimental and numerical hydrodynamic analysis of a stepped planing hull. *Applied Ocean Research*, 64, 135–54. https://doi.org/10.1016/j.apor.2017.02.004

[74] Lotfi, P., Ashrafizaadeh, M., Esfahan, R.K., 2015. Numerical Investigation of A Stepped Planing Hull in Calm Water. *Ocean Engineering*, 94, 103–10. https://doi.org/10.1016/j.oceaneng.2014.11.022

[75] Di Caterino, F., Niazmand Bilandi, R., Mancini, S., Dashtimanesh, A., de Carlini, M., 2018. A numerical way for a stepped planing hull design and optimization. *Technology and Science for the Ships of the Future-Proceedings of NAV 2018: 19th International Conference on Ship and Maritime Research*, 20-22 June, Trieste, Italy, 220-229. https://doi.org/10.3233/978-1-61499-870-9-220

[76] Matveev, K.I., 2012. Two-dimensional modeling of stepped planing hulls with open and pressurized air cavities. *International Journal of Naval Architecture and Ocean Engineering*, 4(2), 162–71. https://doi.org/10.2478/IJNAOE-2013-0087

[77] Febrian, C.E., Chrismianto, D., Rindho, G., 2018. Analisis Hambatan dan Gaya Angkat dari Modifikasi Stephull dengan Variasi Sudut pada Kapal Pilot Boat 15 Meter ALU Menggunakan Metode CFD. *Jurnal Teknik Perkapalan*, 6(1).

[78] Bilandi, R.N., Dashtimanesh, A., Tavakoli, S., 2020. Hydrodynamic study of heeled double-stepped planing hulls using CFD and 2D+T method. *Ocean Engineering*, 196, 106813. https://doi.org/10.1016/j.oceaneng.2019.106813

[79] Dashtimanesh, A., Tavakoli, S., Sahoo, P., 2017. A simplified method to calculate trim and resistance of a two-stepped planing hull. *Ships and Offshore Structures*, 12(sup1), S317–29. https://doi.org/10.1080/17445302.2016.1262809

[80] Dashtimanesh, A., Esfandiari, A., Mancini, S., 2018. Performance Prediction of Two-Stepped Planing Hulls Using Morphing Mesh Approach. *Journal of Ship Production and Design*, 34(03), 236–48. https://doi.org/10.5957/JSPD.160046

[81] Bilandi, R.N., Vitiello, L., Mancini, S., Nappo, V., Roshan, F., Tavakoli, S., Dashtimanesh, A., 2020. Calm-water Performance of A Boat with Two Swept Steps at High-Speeds: Laboratory Measurements and Mathematical Modeling. *Procedia Manufacturing*, Elsevier B.V. 42(2019), 467–74. https://doi.org/10.1016/j.promfg.2020.02.046

[82] Batchelor, G.K., Young, A.D., 1968. An Introduction to Fluid Mechanics. *Journal of Applied Mechanics*, 35(3), 624–624. https://doi.org/10.1115/1.3601282

[83] Ferziger, J.H., Perić, M., 2002. Computational Methods for Fluid Dynamics. Computational Methods for Fluid Dynamics. https://doi.org/10.1007/978-3-642-56026-2

[84] Hirt, C.., Nichols, B.., 1981. Volume of fluid (VOF) method for the dynamics of free boundaries. *Journal of Computational Physics*, 39(1), 201–25. https://doi.org/10.1016/0021-9991(81)90145-5

[85] Shih, T.-H., Liou, W.W., Shabbir, A., Yang, Z., Zhu, J., 1995. A new k-ϵ eddy viscosity model for high reynolds number turbulent flows. *Computers & Fluids*, 24(3), 227–38. https://doi.org/10.1016/0045-7930(94)00032-T

[86] ITTC, 2014. ITTC – Recommended Procedures and Guidelines - Practical guidelines for ship CFD applications. 7.5-03-02-03 (Revision 01).

[87] Hosseini, A., Tavakoli, S., Dashtimanesh, A., Sahoo, P.K., Kõrgesaar, M., 2021. Performance Prediction of a Hard-Chine Planing Hull by Employing Different CFD Models. *Journal of Marine Science and Engineering*, 9(5), 481. https://doi.org/10.3390/jmse9050481

[88] Doustdar, M.M., Kazemi, H., 2019. Effects of fixed and dynamic mesh methods on simulation of stepped planing craft. *Journal of Ocean Engineering and Science*, 4(1), 33–48. https://doi.org/10.1016/j.joes.2018.12.005

[89] Fathuddiin, A., Samuel, S., Kiryanto, K., Widyandari, A., 2020. Prediksi Hambatan Kapal dengan Menggunakan Metode Overset Mesh pada Kapal Planing Hull. *Jurnal Rekayasa Hijau*, 4(1), 24–34. https://doi.org/10.26760/jrh.v4i1.24-34

[90] ANSYS, 2014. Introduction to ANSYS Fluent. Lecture 7: Turbulence Modeling. ANSYS User Manual.

[91] Avci, A.G., Barlas, B., 2018. An Experimental and Numerical Study of a High Speed Planing Craft with Full-Scale Validation. *Journal of Marine Science and Technology (Taiwan)*, 26(5), 617–28. https://doi.org/10.6119/JMST.201810_26(5).0001

[92] ITTC, 2017. ITTC – Recommended Procedures and Guidelines - Resistance and Propulsion Test and Performance Prediction with Skin Frictional Drag Reduction Techniques. 7.5-02-02-03.

[93] Richardson, L.F., 1911. The approximate arithmetical solution by finite differences of physical problems

involving differential equations, with an application to the stresses in a masonry dam. *Philosophical Transactions of the Royal Society A: Mathematical, Physical, and Engineering Sciences*, 210(459–470), 307–57. https://doi.org/10.1098/rsta.1911.0009

[94] Celik, I.B., Ghia, U., Roache, P.J., Freitas, C.J., Coleman, H., Raad, P.., 2008. Procedure for Estimation and Reporting of Uncertainty Due to Discretization in CFD Applications. *Journal of Fluids Engineering*, 130(7), 078001. https://doi.org/10.1115/1.2960953

[95] ITTC, 2010. The Specialist Committee on High Speed Craft Final Report and Recommendations to the 26th ITTC. Rio de janeiro, Brazil.

[96] ITTC, 2008. ITTC – Recommended Procedures and Guidelines - Uncertainty Analysis in CFD Verification and Validation Methodology and Procedures. 7.5-03-01-01.

Submitted: 18.01.2023.
Accepted: 17.07.2023.

Andi Trimulyono
Muhammad Luqman Hakim*, mluqmanhak@lecturer.undip.ac.id
Chairizal Ardhan
Syaiful Tambah Putra Ahmad
Tuswan Tuswan
Ari Wibawa Budi Santosa

Department of Naval Architecture, Faculty of Engineering, Universitas Diponegoro, Semarang, Indonesia 50275